MNRAS 000, 1–14 (2021) Preprint 19 December 2021 Compiled using MNRAS LATEX style file v3.0

X-ray bounds on cooling, composition, and magnetic field of the Cassiopeia A neutron star and young central compact objects

Wynn C. G. Ho[1]★, Yue Zhao[2], Craig O. Heinke[2], D. L. Kaplan[3], Peter S. Shternin[4], and M. J. P. Wijngaarden[5]

[1]*Department of Physics and Astronomy, Haverford College, 370 Lancaster Avenue, Haverford, PA, 19041, USA*
[2]*Department of Physics, University of Alberta, CCIS 4-183, Edmonton, AB T6G 2E1, Canada*
[3]*Center for Gravitation, Cosmology, and Astrophysics, Department of Physics, University of Wisconsin-Milwaukee, P.O. Box 413, Milwaukee, WI 53201, USA*
[4]*Ioffe Institute, Politekhnicheskaya 26, St Petersburg, 194021, Russia*
[5]*Mathematical Sciences and STAG Research Centre, University of Southampton, Southampton SO17 1BJ, UK*

Accepted 2021 July 16. Received 2021 July 16; in original form 2021 March 16

ABSTRACT

We present analysis of multiple *Chandra* and *XMM-Newton* spectra, separated by 9–19 years, of four of the youngest central compact objects (CCOs) with ages < 2500 yr: CXOU J232327.9+584842 (Cassiopeia A), CXOU J160103.1−513353 (G330.2+1.0), 1WGA J1713.4−3949 (G347.3−0.5), and XMMU J172054.5−372652 (G350.1−0.3). By fitting these spectra with thermal models, we attempt to constrain each CCO's long-term cooling rate, composition, and magnetic field. For the CCO in Cassiopeia A, 14 measurements over 19 years indicate a decreasing temperature at a ten-year rate of 2.2 ± 0.2 or 2.8 ± 0.3 percent (1σ error) for a constant or changing X-ray absorption, respectively. We obtain cooling rate upper limits of 17 percent for CXOU J160103.1−513353 and 6 percent for XMMU J172054.5−372652. For the oldest CCO, 1WGA J1713.4−3949, its temperature seems to have increased by 4 ± 2 percent over a ten year period. Assuming each CCO's preferred distance and an emission area that is a large fraction of the total stellar surface, a non-magnetic carbon atmosphere spectrum is a good fit to spectra of all four CCOs. If distances are larger and emission areas are somewhat smaller, then equally good spectral fits are obtained using a hydrogen atmosphere with $B \leq 7 \times 10^{10}$ G or $B \geq 10^{12}$ G for CXOU J160103.1−513353 and $B \leq 10^{10}$ G or $B \geq 10^{12}$ G for XMMU J172054.5−372652 and non-magnetic hydrogen atmosphere for 1WGA J1713.4−3949. In a unified picture of CCO evolution, our results suggest most CCOs, and hence a sizable fraction of young neutron stars, have a surface magnetic field that is low early in their life but builds up over several thousand years.

Key words: dense matter – ISM: individual: Cassiopeia A, G330.2+1.0, G347.3−0.5, G350.1−0.3 – stars: individual: CXOU J160103.1−513353, 1WGA J1713.4−3949, XMMU J172054.5−372652– stars: neutron – supernovae: individual: Cassiopeia A – X-rays: stars

1 INTRODUCTION

Central compact objects (CCOs) form a class of young neutron stars that are found near the center of a supernova remnant, possess relatively steady long-term thermal X-ray surface emission, and are not clearly detected at other energies (De Luca 2008, 2017; Gotthelf et al. 2013a). Three of the most notable CCOs are those in supernova remnants (SNRs) 1E 1207.4−5209, Kesteven 79, and Puppis A, which are the only three thus far with a measured spin period (P = 424, 105, and 112 ms, respectively). The 340 yr old SNR Cassiopeia A (Fesen et al. 2006) hosts another important CCO, one that is apparently rapidly decreasing in temperature at a rate of $\lesssim 3$ percent per decade (Heinke & Ho 2010; Posselt & Pavlov 2018; Wijngaarden et al. 2019), which is naturally explained by and provides direct evidence of proton superconductivity and neutron superfluidity in the core of the neutron star (Page et al. 2011; Shternin et al. 2011), although other explanations or contributions are possible (see, e.g., Yang et al. 2011 for r-mode oscillations, Blaschke et al. 2012 for slower thermal relaxation, Negreiros et al. 2013; Taranto et al. 2016 for rotation-induced and fast cooling, Noda et al. 2013; Sedrakian 2013 for phase transitions, Bonanno et al. 2014 for magnetic field decay, and Leinson 2014; Hamaguchi et al. 2018 for axion cooling).

To model and interpret CCO spectra, it is important to know the composition of the thin atmosphere that covers the neutron star surface (Potekhin 2014). Because of rapid gravitational settling of heavy elements, the surface is composed of the lightest elements present (Alcock & Illarionov 1980). For isolated or non-accreting binary systems, a hydrogen atmosphere is likely due to even a small amount of accretion from the interstellar medium (Blaes et al. 1992). Helium or carbon atmospheres are possible for the youngest neutron stars that are still hot after formation since hydrogen and helium can be depleted by residual nuclear burning (Chang & Bildsten 2003, 2004; Chang et al. 2010; Wijngaarden et al. 2019, 2020). Such appears to be the case for the CCO in Cassiopeia A, i.e, its observed properties

★ E-mail: wynnho@slac.stanford.edu

Table 1. Properties of CCOs studied here. Note that pulsed fraction is not defined consistently among referenced works. See text for details and references.

CCO	SNR	Age (yr)	d (kpc)	Pulsation search results	
				Pulsed fraction	Search range
CXOU J160103.1−513353	G330.2+1.0	< 1000	5–11.3	< 0.40	$P > 12.5$ ms
				< 0.21	147 ms < P < 100 s
1WGA J1713.4−3949	G347.3−0.5	1500–2300	1.3 ± 0.4	not given	3 ms < P < 10 ms
				< 0.25	7.8 ms < P < 100 s
				< 0.04	400 ms < P < 100 s
XMMU J172054.5−372652	G350.1−0.3	< 600	4.5–10.7	< 0.33	146 ms < P < 1.8 s
				< 0.20	1.8 s < P < 1 hr
CXOU J232327.9+584842	Cassiopeia A	340 ± 19	$3.4^{+0.3}_{-0.1}$	< 0.12	$P > 10$ ms

are well-described by a carbon atmosphere, the presence of which can be understood given the youth of the CCO (Chang et al. 2010; Wijngaarden et al. 2019). In recent years, a few other CCOs are suggested to also have carbon atmospheres (Klochkov et al. 2013, 2015, 2016; Suleimanov et al. 2017; Doroshenko et al. 2018; Hebbar et al. 2020; Potekhin et al. 2020), although it is important to note that these CCOs/SNRs are likely to be much older than Cassiopeia A.

Another important property of CCOs is their magnetic field B, which, as a class, is uncertain. From their timing properties, the magnetic fields of the three CCOs with a measured spin period noted above are inferred to be $\sim 3 \times 10^{10} - 10^{11}$ G (Halpern & Gotthelf 2010; Gotthelf et al. 2013a), and that of 1E 1207.4−5209 is in approximate agreement with the field inferred from an electron cyclotron interpretation of features in its observed spectrum (Sanwal et al. 2002; Bignami et al. 2003; De Luca et al. 2004). Meanwhile, non-detection of pulsations from the CCO in Cassiopeia A (Murray et al. 2002; Ransom 2002; Pavlov & Luna 2009; Halpern & Gotthelf 2010) suggests its observed X-rays are due to emission from the entire hot stellar surface, which produces a spectrum well-fit by a low magnetic field carbon atmosphere (Ho & Heinke 2009). The low inferred magnetic field of these CCOs could be the result of birth at these field strengths. Alternatively, large and rapid mass accretion soon after a supernova explosion (Chevalier 1989) can bury an initial surface field and lead to the field's gradual emergence at the present time (Ho 2011, 2013).

Here we examine *Chandra* and *XMM-Newton* CCD spectra of three CCOs (see Table 1) that are possibly the next youngest to the CCO in Cassiopeia A: CXOU J160103.1−513353 with an age of < 1000 yr (Borkowski et al. 2018), 1WGA J1713.4−3949 with an age of $\sim$ 1500 − 2300 yr (Tsuji & Uchiyama 2016; Acero et al. 2017), and XMMU J172054.5−372652 with an age of < 600 yr (Borkowski et al. 2020). *Chandra* spectra of each CCO are taken approximately nine to fourteen years apart, and *XMM-Newton* spectra of 1WGA J1713.4−3949 span either thirteen years for EPIC-MOS or ten years for EPIC-pn (see Table 2). These *Chandra* ACIS data are all the publically-available data on each of these CCOs; similarly for *XMM-Newton* data on 1WGA J1713.4−3949. We do not examine here two *XMM-Newton* observations of CXOU J160103.1−513353 taken in 2008 and 2015 since they have a shorter time separation (7 years) than our *Chandra* data (11 years) and are analyzed in previous work (see, e.g., Doroshenko et al. 2018). We also do not examine the single *XMM-Newton* observation of XMMU J172054.5−372652 taken in 2007 (see Gaensler et al. 2008). While the first epoch *Chandra* CCO spectra considered here are well-studied (similarly for the first epoch *XMM-Newton* spectra and 2014 pn spectrum of 1WGA J1713.4−3949; see references below), the later epoch CCO spectra have not been previously analyzed (see Borkowski et al. 2018, 2020 for analyses of the spectra of SNRs G330.2+1.0 and G350.1−0.3 using the observations examined here). Therefore our work is the first that we are aware to investigate the possibility of long-term variability of each of these CCOs. Using all epochs of data, we attempt to constrain the cooling rate and infer properties of each CCO, in particular their surface composition and magnetic field. We also update Wijngaarden et al. (2019) with spectral measurements and fits of the CCO in Cassiopeia A, including the most recent *Chandra* observation from 2019 and using the latest improvements in ACIS calibration, especially contaminant model N0014, which improves upon N0010 used by Posselt & Pavlov (2018) and N0012 used by Wijngaarden et al. (2019) (see Section 3).

An outline of the paper is as follows. Section 2 provides some details and summarizes relevant previous works on the four young CCOs examined here. Section 3 describes our procedure for analyzing *Chandra* and *XMM-Newton* spectra of the four CCOs: CXOU J160103.1−513353, 1WGA J1713.4−3949, XMMU J172054.5−372652, and Cassiopeia A. Section 4 presents our spectral fits. Section 5 summarizes and discusses implications of our results in the context of neutron star cooling and the CCO class of neutron stars.

2 SUMMARY OF FOUR CCOS

The first CCO we consider, CXOU J160103.1−513353, is in SNR G330.2+1.0 (Park et al. 2006) at a distance $d > 4.9 \pm 0.3$ kpc (McClure-Griffiths et al. 2001), with a possible upper limit of 11.3 kpc (Torii et al. 2006), although Borkowski et al. (2018) argue against $d \gtrsim 10$ kpc. From measurements of shell expansion, the SNR age is found to be < 1000 yr (Borkowski et al. 2018). Pulsation searches yield pulsed fraction limits of 40 percent for spin periods $P > 12.5$ ms using 2008 *XMM-Newton* data (Park et al. 2009) and 21 percent for 147 ms < P < 100 s using 2008 and 2015 *XMM-Newton* data (Doroshenko et al. 2018). Doroshenko et al. (2018) use a two-component (hot spot and cool entire surface) emission model to argue that there is a 30 percent probability the viewing geometry is not favorable for detecting pulsations. Spectrally, Park et al. (2006) analyzed the early epoch *Chandra* data studied here (ObsID 6687), Park et al. (2009) performed a joint fit with 2008 *XMM-Newton* spectra, and Doroshenko et al. (2018) fit only the 2008 *XMM-Newton* spectra along with subsequent *XMM-Newton* data from 2015 using non-magnetic hydrogen and carbon atmosphere spectra and did not search for temperature variations between the 2008 and 2015 data. While power law and thermal blackbody or atmosphere model spectra can each fit the observed spectra of CXOU J160103.1−513353, the power law model is disfavored because of a large index $\Gamma \gtrsim 5$ and high absorption $N_{\rm H} \approx 5.4 \times 10^{22}$ cm^{-2} (Park et al. 2009). The latter can be compared to $N_{\rm H} \approx (2-3) \times 10^{22}$ cm^{-2} from spectral analysis

Table 2. X-ray observations of four CCOs.

ObsID	Date	Exposure (ks)	Frame time (s)	Pile-up fraction
CXOU J160103.1−513353 (*Chandra* ACIS-I)				
6687	2006 May 22	50	3.24	0.02
19163	2017 May 2	74	3.14	0.01
20068	2017 May 5	74	3.14	0.01
1WGA J1713.4−3949 (*Chandra* ACIS-I)				
736	2000 July 25	30	3.24	0
5559[a]	2005 April 19	9.6	3.24	0.30
15967	2014 July 6	29	0.94	0.03
1WGA J1713.4−3949 (*XMM-Newton* EPIC)				
0093670501[b]	2001 March 2	15	2.6/0.2	0
0207300201[c]	2004 February 22	34	2.6/0.006	0
0722190101[d]	2013 August 24	139	0.002/0.006	0
0740830201[c]	2014 March 2	141	2.6/0.006	e
XMMU J172054.5−372652 (*Chandra* ACIS-S)				
10102	2009 May 22	83	3.24	0.06
14806	2013 May 11	89	0.00285	f
20312	2018 July 2	41	3.14	0.05
20313	2018 July 4	20	3.14	0.05
21120	2018 July 5	38	3.14	0.05
21119	2018 July 7	48	3.14	0.05
21118	2018 July 8	43	3.14	0.05
Cassiopeia A (*Chandra* ACIS-S Graded)				
114	2000 Jan 30	50	3.24	0.13
1952	2002 Feb 6	50	3.24	0.13
5196	2004 Feb 8	50	3.24	0.13
9117	2007 Feb 5	25	3.04	0.11
9773	2007 Feb 8	25	3.04	0.12
10935	2009 Nov 2	23	3.04	0.11
12020	2009 Nov 3	22	3.04	0.11
10936	2010 Oct 31	32	3.04	0.11
13177	2010 Nov 2	17	3.04	0.11
14229	2012 May 15	49	3.04	0.08
14480	2013 May 20	49	3.04	0.10
14481	2014 May 12	49	3.04	0.10
14482	2015 Apr 30	49	3.04	0.07
19903	2016 Oct 20	25	3.04	0.08
18344	2016 Oct 21	26	3.04	0.09
19604	2017 May 16	50	3.04	0.07
19605	2018 May 15	49	3.04	0.07
19606	2019 May 13	49	3.04	0.06

[a] Not used here due to 30 percent pile-up fraction. Used by Mignani et al. (2008) only to determine position of CCO.
[b] MOS/pn in full frame/extended full frame mode; pn not used here.
[c] MOS/pn in full frame/small window mode.
[d] MOS/pn in timing/small window mode; MOS not used here.
[e] Pile-up fraction of 0.03 for MOS1 and 0 for MOS2 and pn.
[f] Not used here due to continuous-clocking mode.

of the SNR using *ASCA*, *Chandra*, and *XMM-Newton* (Torii et al. 2006; Park et al. 2009; Williams et al. 2018).

The second CCO, 1WGA J1713.4−3949, is in SNR G347.3−0.5 (also known as RX J1713.7−3946) (Slane et al. 1999) at a distance of ∼ 1 kpc (see, e.g., Fukui et al. 2003; Koo et al. 2004; Moriguchi et al. 2005). Here we adopt $d = 1.3 \pm 0.4$ kpc from Cassam-Chenaï et al. (2004) for simplicity. While the association of the SNR with the historical supernova SN 393 is uncertain (Wang et al. 1997; Fesen et al. 2012), expansion of the remnant indicates an age ∼ 1500 – 2300 yr (Tsuji & Uchiyama 2016; Acero et al. 2017). Pulsation searches provide a pulsed fraction limit of 25 percent for 7.8 ms $< P <$ 100 s using *RXTE* and a limit of 4 percent for 0.4 s $< P <$ 100 s using *XMM-Newton* (Lazendic et al. 2003) and no detection for 3 ms $< P <$ 10 ms using *XMM-Newton* (Papa et al. 2020). No optical/IR counterpart is detected (Mignani et al. 2008). Cassam-Chenaï et al. (2004) fit the earliest epoch *XMM-Newton* MOS and pn spectra used here (ObsID 0093670501) with either a power law or thermal model, Lazendic et al. (2003) performed a joint fit with the above *XMM-Newton* spectra and the early epoch *Chandra* spectrum used here (ObsID 736), and Potekhin et al. (2020) fit only the 2014 *XMM-Newton* pn spectrum (ObsID 0740830201). Like in the case of CXOU J160103.1−513353, a large inferred power law index $\Gamma = 4.2$ and high absorption $N_{\rm H} = 11 \times 10^{21}$ cm^{-2} argue for a thermal model. The absorption can be compared to $N_{\rm H} \sim 5 \times 10^{21}$ cm^{-2} for regions of the SNR near the CCO (Cassam-Chenaï et al. 2004; Acero et al. 2009).

The third CCO, XMMU J172054.5−372652, is in SNR G350.1−0.3 (Gaensler et al. 2008). The distance is estimated to be 4.5 kpc from a possible molecular cloud association, 4.5–10.7 kpc from H I absorption in the direction of the SNR (Gaensler et al. 2008), or ∼ 9 kpc from using the interstellar gas density (Yasumi et al. 2014). Free expansion of the SNR gives an age 600–1200 yr (Lovchinsky et al. 2011), while ejecta motion yields an age < 600 yr (Borkowski et al. 2020), in agreement with that obtained from forward and reverse shock modeling of the SNR (Leahy et al. 2020). Pulsation searches using *XMM-Newton* yield pulsed fraction limits of 33 percent for 146 ms $< P <$ 1.8 s and 20 percent for 1.8 s $< P <$ 1 hr (Gaensler et al. 2008). Either a power law or blackbody model can fit the CCO spectra from *XMM-Newton* (Gaensler et al. 2008) and *Chandra* (ObsID 10102; Lovchinsky et al. 2011). Like in the other CCOs studied here, the large inferred $\Gamma \approx 5.5$ disfavors the power law model.

The last CCO we consider is the one in the Cassiopeia A SNR discussed above (also known as CXOU J232327.9+584842; Tananbaum 1999; hereafter we do not necessarily distinguish between the CCO and SNR). The distance to the SNR is $3.4^{+0.3}_{-0.1}$ kpc (Reed et al. 1995), and expansion of the remnant gives a supernova explosion date of 1681 ± 19 (Fesen et al. 2006), such that the SNR age is ≈ 340 yr. The strongest limit on the pulsed fraction of the CCO is 12 percent for $P >$ 10 ms using *Chandra* HRC (Halpern & Gotthelf 2010). In addition to carbon atmosphere model fits to the CCO spectra, a power law model with $\Gamma \approx 5$ or hydrogen atmosphere models can also fit the spectra (Pavlov & Luna 2009; Ho & Heinke 2009; Posselt et al. 2013).

3 SPECTRAL ANALYSIS OF *Chandra* AND *XMM-Newton* DATA

A summary of *Chandra* and *XMM-Newton* observations used in this work is shown in Table 2. Note that 1WGA J1713.4−3949 is far off-axis and on the ACIS-I S1 chip in the 2000 observation (see Figure 1 of Lazendic et al. 2003).

We reprocess all *Chandra* data with `chandra_repro` and Chandra Interactive Analysis of Observations (CIAO) 4.13 and Calibration Database (CALDB) 4.9.4 (Fruscione et al. 2006). Examination of the lightcurve (100 s bins) of each observation provides no indication of background flares. Spectra are extracted using `specextract`. For CXOU J160103.1−513353, source counts are taken from a ≈2.″5 radius circle centered very near the CCO position determined by Park et al. (2006) using ObsID 6687, i.e., R.A. = $16^{\rm h}01^{\rm m}03\overset{\rm s}{.}14$, decl. = −51°33′53.″6 (J2000), while background for the source is

taken from a 3″–5″ radius circular annulus around the CCO. The resulting background-subtracted source counts are ∼ 640, 710, and 720 counts for ObsIDs 6687, 19163, and 20068, respectively. Since ObsIDs 19163 and 20068 are taken within a few days of each other, we use `combine_spectra` and `dmgroup` to merge spectra extracted from these two observations for a total exposure of 148 ks. Spectra are binned with a minimum of 25 counts per energy bin. Using `pileup_map`, we find a pile-up fraction of < 2 percent (see Table 2).

For *Chandra* data of 1WGA J1713.4−3949, source counts are taken from a region centered at the CCO position determined by Mignani et al. (2008) using ObsID 5559, i.e., R.A. = $17^{\rm h}13^{\rm m}28\overset{\rm s}{.}32$, decl. = −39°49′53″.34 (J2000). For ObsID 736, the CCO is very far off-axis and is extremely distended. Therefore, we use a 37″×61″ radius elliptical region tilted at 30° to extract source counts and a 2′×3′ radius elliptical region tilted at 30° and about 4′ north of the CCO for the background; these regions are similar to those used in Lazendic et al. (2003). For ObsID 15967, we use a 6″×10″ radius elliptical region tilted at 120° to extract source counts and a 11″–20″ radius circular annulus around the CCO for the background. The resulting background-subtracted source counts are ∼ 11000 counts each for ObsID 736 and 15967. Spectra are binned with a minimum of 50 counts per energy bin. We find negligible pile-up for ObsID 736 and a pile-up fraction of < 3 percent for ObsID 15967.

For *XMM-Newton* observations of 1WGA J1713.4−3949, we only consider EPIC spectra measured using the same detector mode, i.e., full frame for MOS and small window for pn (see Table 2), in order to reduce systematic uncertainties. We use *XMM-Newton* SCIENCE ANALYSIS SOFTWARE (SAS) 19.0.0 to reduce observation data files (ODFs) for extraction of spectra. We process EPIC-MOS and pn ODFs using `emproc` and `epproc`, respectively, to generate calibrated and concatenated event files. To clean these files of flaring events, we first extract high-energy (10–12 keV) and single-event (PATTERN=0) light curves, from which we determine count rate upper limits for low and steady background and MOS and pn count-rates of 0.13 counts s^{-1} and 0.25 counts s^{-1} for the 2001 dataset, 0.28 counts s^{-1} and 0.07 counts s^{-1} for the 2004 dataset, 0.13 counts s^{-1} and 0.05 counts s^{-1} for the 2013 dataset, and 0.15 counts s^{-1} and 0.02 counts s^{-1} for the 2014 dataset. These count rates are then input into the `tabgtigen` tool to generate corresponding good time intervals (GTIs), which are then input into the `evtselect` tool to produce flare-cleaned event files. From the cleaned event files, we extract MOS and pn spectra using a 30″ circular region centred on the above-mentioned source position. For all MOS full-frame observations, we select for background a 30″ circular region centered at R.A. = $17^{\rm h}13^{\rm m}13^{\rm s}$, decl. = −39°47′58″ (J2000), about 3.′5 northwest of the source. In the 2004 and 2014 observations, the source is close to the bottom edge of the pn field-of-view, and we choose a circular background region centered at R.A. = $17^{\rm h}13^{\rm m}36^{\rm s}$, decl. = −39°47′56″, about 2.′5 northeast of the source. In the 2013 observation, the source is close to the top edge of the pn field-of-view, and we select a different location at R.A. = $17^{\rm h}13^{\rm m}21^{\rm s}$, decl. = −39°51′54″ for background extraction, but it has the same offset (2.′5) from the source. Since non-thermal X-ray emission from the SNR is at a relatively low level compared to the CCO emission (Katsuda et al. 2015), we find a < 1 percent effect on the final results by using different background regions. Spectra are binned with a minimum of 30 counts per energy bin for the shorter 2001 and 2004 observations and 100 counts per energy bin for the longer 2013 and 2014 observations. Data from MOS1, MOS2, and pn have negligible pile-up, except for the 2014 MOS1 data which have an estimated pile-up fraction of < 3 percent.

For *Chandra* data of XMMU J172054.5−372652, source counts are taken from a ≈2.″5 radius circle centered very near the CCO position determined by Gaensler et al. (2008) using *XMM-Newton*, i.e., R.A. = $17^{\rm h}20^{\rm m}54\overset{\rm s}{.}5$, decl. = −37°26′52″ (J2000), while background for the source is taken from a 3″–5″ radius circular annulus around the CCO. The resulting background-subtracted source counts are ∼ 3800, 1700, 830, 1600, 2000, and 1900 counts for ObsIDs 10102, 20312, 20313, 21120, 21119, and 21118, respectively. Since ObsIDs 20312-3 and 21118-20 are all taken within a week of each other, we merge spectra extracted from these observations for a total exposure of 189 ks. Spectra are binned with a minimum of 50 counts per energy bin. We find a pile-up fraction of 5–6 percent (see Table 2).

For *Chandra* data of the CCO in Cassiopeia A, source counts are taken from a ≈2″ radius circle centered on the CCO, while background for the source is taken from a 2.″5–4″ radius circular annulus around the CCO. We merge spectra from observations taken within a few days of each other (i.e., ObsIDs 9117 and 9773, 10935 and 12020, 10936 and 13177, and 19903 and 18344). Spectra are binned with a minimum of 25 counts per energy bin. Table 2 shows the estimated pile-up fraction for each observation. We note that `CALDB` 4.9.4 includes the latest ACIS contaminant model N0014, which corrects for the decreasing quantum efficiency of ACIS at low energies[1].

We perform spectral fitting using Xspec 12.11.0 (Arnaud 1996). We account for pile-up (Davis 2001) in *Chandra* data by allowing the grade migration parameter α to be fit for each observation (unless specified differently below) and setting the frame time for each observation to that given in Table 2, maximum number of photons to 5, and point-spread-function fraction to 0.95. As noted in Section 1, a power law could be used to model spectra of each CCO, but the implied index of $\Gamma > 4$ in each case indicates thermal models are more appropriate. Thus, in the present work, we only consider absorbed thermal models consisting of `tbabs` and either `bbodyrad`, `nsatmos`, `nsx`, or `nsmaxg`. The former models photoelectric absorption in the interstellar medium, and we use abundances from Wilms et al. (2000) and cross-sections from Verner et al. (1996). The thermal component models intrinsic emission from the CCO as either a blackbody or neutron star atmosphere spectrum. The simplest model is a blackbody (`bbodyrad`), and we give its corresponding fit results primarily as a comparison to results from previous works.

Thermal emission from a neutron star is more correctly described by models that account for the properties of the atmosphere that covers the stellar surface, in particular the magnetic field and composition of the atmosphere (Potekhin 2014). We consider atmosphere models that are either non-magnetic (applicable when $B \lesssim 10^9$ G) or magnetic (with a single B in the range 10^{10} G ≤ B ≤ 3×10^{13} G), and these are listed in Table 3. The four spectral models with varying magnetic field and surface temperature (via `nsmaxg`; see Ho et al. 2008) do not fit the data well and will not be discussed further. For composition, partially ionized carbon, oxygen, and neon spectral models at 10^{12} and 10^{13} G (Mori & Ho 2007) fit the data

Table 3. Neutron star atmosphere models used for spectral fits in Section 4. See text for other models considered.

Model	Composition	Magnetic field
`nsatmos`	H	non-magnetic
`nsx`	C	non-magnetic
`nsmaxg`	H	$10^{10} - 3\times10^{13}$ G

[1] https://cxc.harvard.edu/caldb/downloads/Release_notes/CALDB_v4.9.4.

poorly, so will also not be discussed further. On the other hand, non-magnetic hydrogen (`nsatmos`; Heinke et al. 2006) and carbon (`nsx`; Ho & Heinke 2009) spectral models fit the data well, as do partially ionized hydrogen models at a number of single magnetic field values (`nsmaxg`; Ho et al. 2008; Ho 2014; Potekhin et al. 2014). We note that, while non-magnetic helium (via `nsx`) yields fits that are comparable to those of non-magnetic hydrogen in the cases of CXOU J160103.1−513353 and XMMU J172054.5−372652 and are poorer fits in the case of 1WGA J1713.4−3949, we do not give their results in the following sections since a helium atmosphere is unlikely to be present for isolated neutron stars at the age and temperature of these CCOs (Chang et al. 2010; Wijngaarden et al. 2019).

For each absorbed thermal atmosphere model, as well as absorbed blackbody model, there are three model fit parameters: X-ray absorption $N_{\rm H}$, temperature T, and normalization $R_{\rm em}/d$ (where applicable, we normalize the emission radius $R_{\rm em}$ to a neutron star radius $R = 12$ km and normalize the distance d to the nominal distance for each CCO). Each fit parameter can be fit jointly between all observations, so that there is only one best-fit value for each model and source, or fit individually for each observation of a source. For each CCO studied here, except Cassiopeia A, we first perform spectral fits with all three parameters jointly fit to all data, and the fit statistic χ^2 is computed for each fit. This is done for each model shown in Table 3: non-magnetic hydrogen (`nsatmos`) and carbon (`nsx`) and magnetic hydrogen (`nsmaxg`). For `nsmaxg`, models available in Xspec are at single magnetic field strengths of $B = 10^{10}, 4\times10^{10}, 7\times10^{10}, 10^{11}, 10^{12}, 2\times10^{12}, 4\times10^{12}, 7\times10^{12}, 10^{13}, 2\times10^{13}, 3\times10^{13}$ G; we perform fits with each one of these `nsmaxg` models but only show results for the one or two with the lowest χ^2. Next, we perform fits which allow only one of the three fit parameters to vary between each observation, and we cycle through each parameter, i.e., first $N_{\rm H}$ is allowed to vary while T and $R_{\rm em}/d$ are the same between observations, then T is allowed to vary while $N_{\rm H}$ and $R_{\rm em}/d$ are the same, and finally $R_{\rm em}/d$ is allowed to vary while $N_{\rm H}$ and T are the same. We use the F-test to compare the resulting χ^2 of the fits to determine if allowing one fit parameter to vary improves the fit sufficiently to justify the decrease in number of degrees of freedom (dof). Then we perform fits which allow two of the three fit parameters to vary between each observation, and we cycle through each pair of parameters and use the F-test to evaluate if the improvement is significant. Finally, we perform a fit which allows all three fit parameters to vary and evaluate if the improvement is significant. Results shown in the tables in Section 4 are those where the F-test justifies the number of independent fit parameters.

For modeling the spectra of the CCO in Cassiopeia A, we consider only a carbon atmosphere model, since other models are studied in previous works (Pavlov & Luna 2009; Ho & Heinke 2009; Posselt et al. 2013), and we fix the distance to 3.4 kpc and normalization to 1 (i.e., detected X-rays are from entire neutron star surface). We also include a component `spexpcut`, with exponent index = −2 and characteristic energy $E_{\rm cut}({\rm keV}) = [0.49\,N_{\rm H}(10^{22}\ {\rm cm}^{-2})]^{1/2}$, to model interstellar scattering (Predehl et al. 2003), as done in our previous works; however its inclusion has a minimal effect on the fits at the spectral resolution of the Cassiopeia A data (see, e.g., Posselt et al. 2013). Because of the last, we do not apply this scattering model to analyses of the other CCO spectra.

4 RESULTS

4.1 CXOU J160103.1−513353

Figure 1 shows the 2006 and (merged) 2017 *Chandra* spectra of CXOU J160103.1−513353, and Table 4 shows results of model fits of these spectra in the energy range 1.2–6 keV where there are sufficient numbers of counts. Even though we find the pile-up grade migration parameter α to be unconstrained in all fits of the spectra, we leave it free to vary since it has an (small) effect on the uncertainties of other fit parameters. We see that when we assume all other spectral model parameters ($N_{\rm H}$, T, and $R_{\rm em}/d$) are linked and thus constant between 2006 and 2017, the resulting emission region size $R_{\rm em}$ for the blackbody fit is only 0.5 km (assuming a distance $d = 5$ kpc to CXOU J160103.1−513353; see below). Such a small emitting region or hot spot would naturally lead to pulsed emission as the neutron star rotates, which is not seen (see Section 1). Of course non-detection could be the result of an unfavorable viewing geometry or a pulsed

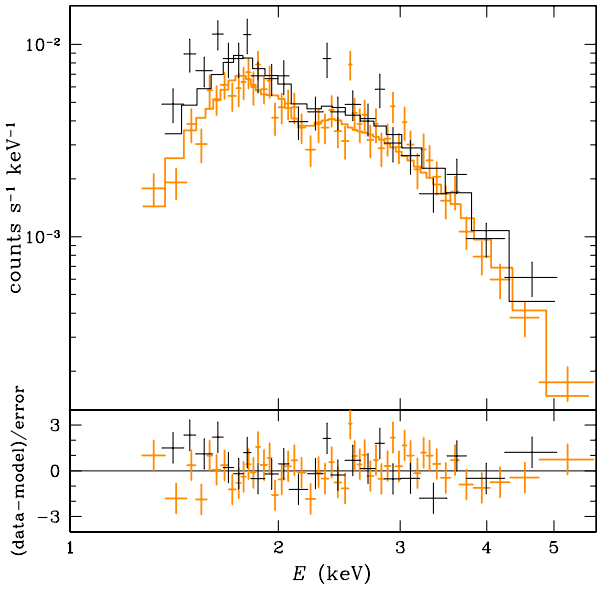

Figure 1. Upper panel shows *Chandra* spectra (black for 2006 and orange for merged 2017 data) of CXOU J160103.1−513353 and absorbed non-magnetic carbon atmosphere model spectra. Model results shown here are from fits with all parameters linked between the two sets of observations. Lower panel shows fit residuals.

Table 4. Results of fits to the 2006 and (merged) 2017 *Chandra* spectra of CXOU J160103.1−513353 at 1.2–6 keV. Along with `pileup` and `tbabs`, fits are performed using model `bbodyrad`, `nsatmos`, `nsx`, or `nsmaxg` with model parameters linked between 2006 and 2017 fits. Other model parameters are fixed at $M = 1.4\,M_\odot$, $R = 12$ km, and $d = 5$ kpc. Errors are 1σ.

$N_{\rm H}$ (10^{22} cm^{-2})	T (10^6 K)	$R_{\rm em}/R$ or 5 kpc/d	$f^{\rm abs}_{1.2-6}$ (10^{-13} erg cm^{-2} s^{-1})	χ^2/dof
blackbody				
$3.8^{+0.3}_{-0.3}$	$5.4^{+0.2}_{-0.2}$	$0.044^{+0.005}_{-0.004}$	$1.4^{+0.1}_{-0.2}$	82.9/67
`nsatmos` - non-magnetic hydrogen				
$4.6^{+0.3}_{-0.3}$	$3.0^{+0.2}_{-0.1}$	$0.23^{+0.05}_{-0.03}$	$1.4^{+0.1}_{-0.2}$	83.1/67
`nsx` - non-magnetic carbon				
$4.8^{+0.3}_{-0.3}$	$1.9^{+0.2}_{-0.1}$	$0.75^{+0.23}_{-0.17}$	$1.4^{+0.1}_{-0.2}$	84.2/67
`nsmaxg` - hydrogen at 4×10^{10} G				
$4.5^{+0.3}_{-0.3}$	$3.1^{+0.2}_{-0.2}$	$0.20^{+0.04}_{-0.03}$	$1.4^{+0.1}_{-0.2}$	84.9/67
`nsmaxg` - hydrogen at 10^{13} G				
$4.5^{+0.3}_{-0.3}$	$3.2^{+0.2}_{-0.2}$	$0.21^{+0.05}_{-0.03}$	$1.4^{+0.1}_{-0.3}$	83.2/67

fraction below detection thresholds ($\approx$ 20 percent in the case of CXOU J160103.1−513353 and spin periods comparable to other CCOs; see Table 1).

Very similar quality of fits are achieved using atmosphere models, but in this case, the emission size is much larger ($R_{\rm em} \approx 2-3$ km for hydrogen and $\sim$ 9 km for carbon, assuming a neutron star radius $R = 12$ km) and indicates a significant fraction of the neutron star surface is hot and emitting detectable X-rays. Such large emitting regions can yield low enough amplitude rotational variations to explain non-detection of pulsations (see Section 5). From similar quality of fits, with a difference in fit-statistic $\Delta\chi^2 \approx 1$ for 67 dof, we cannot distinguish between hydrogen and carbon compositions. The same is true for partially ionized hydrogen at magnetic fields $B \le 7\times10^{10}$ G and $B \ge 10^{12}$ G (see examples in Table 4). Our results are in general agreement with those of previous fits to the 2006 *Chandra* spectrum (Park et al. 2006) and *XMM-Newton* spectra (Park et al. 2009; Doroshenko et al. 2018) using a blackbody model, non-magnetic hydrogen atmosphere (`hatm`) and carbon atmosphere (`carbatm`) models, and fully ionized hydrogen atmosphere model (`nsa`) at $B = 0, 10^{12}, 10^{13}$ G (note that the comparison is to the hotter component in two-component hydrogen model fits performed in Park et al. 2009; Doroshenko et al. 2018). We also note that the absorption $N_{\rm H} \sim (4.5-4.8)\times10^{22}$ cm^{-2} inferred for the CCO using atmosphere models is slightly lower than the power law value of $(5.4\pm0.6)\times10^{22}$ cm^{-2} (Park et al. 2009) but still greater than the value $N_{\rm H} \approx (2-3)\times10^{22}$ cm^{-2} inferred from the SNR (see Section 1).

There are two important issues to note regarding the spectral fit results shown in Table 4. The first is that it is not strictly correct to allow only a fraction of the neutron star surface to be fit in Xspec using the available neutron star atmosphere spectral tables, i.e., allowing $R_{\rm em} < R$. This is because these tables are calculated assuming emission from the entire surface, whereas emission from a hot spot reaches an observer only for certain angles of photon propagation, which in turn depend on the location of the spot on the surface and the viewing geometry and is not a simple re-scaling of emission from the whole surface (see, e.g., Bogdanov et al. 2019). However, this inaccuracy will be small when the inferred hot spot is large. The second issue is that each fit assumes the nominal distance to CXOU J160103.1−513353 of 5 kpc, while the distance could be as large as 11.3 kpc (see Section 1), although such a large distance would imply very fast moving supernova ejecta (Borkowski et al. 2018). The distance assumption directly impacts the inferred size of the emission region, i.e., $R_{\rm em} \propto d$. One alternative way of interpreting the spectral fit results then is to increase the distance by a factor of $R/R_{\rm em}$ and assume emission from the entire surface (or a large fraction of it). This would imply a distance to CXOU J160103.1−513353 of $\sim 22\pm3$ kpc for a hydrogen atmosphere or 7 ± 2 kpc for a carbon atmosphere. Although the former exceeds the estimated maximum of 11.3 kpc, this maximum distance can be satisfied if the hydrogen hot spot occupies ~20 percent of the surface instead of the entire surface.

To complete our spectral analysis of CXOU J160103.1−513353, we consider whether model parameters change between the two epochs of *Chandra* observations (see Section 3). The greatest improvement in fit statistics occurs when $N_{\rm H}$ is allowed to vary, with $\Delta\chi^2 \approx 6$ for one fewer degree of freedom and a F-test probability of 0.02–0.03, and fits only improve by $\Delta\chi^2 < 1$ when T varies, with T differences within errors (see Section 5.1). When all parameters are allowed to vary, $\Delta\chi^2 < 12$ and most of the improvement is due to a possible change of $N_{\rm H}$. A F-test between allowing only $N_{\rm H}$ to vary and all parameters to vary has probability of 0.11. Thus we find $N_{\rm H}$ may be varying, but the evidence is not conclusive.

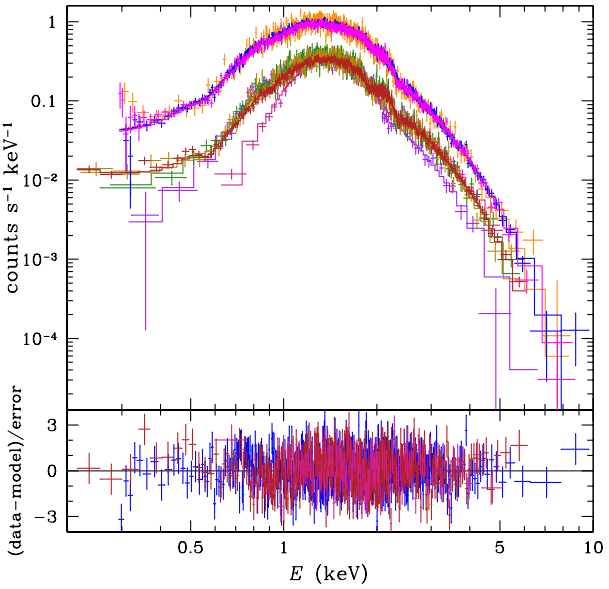

Figure 2. Upper panel shows *Chandra* ACIS spectra and *XMM-Newton* MOS and pn spectra of 1WGA J1713.4−3949 and absorbed non-magnetic carbon atmosphere model spectra (top three are pn, middle three are MOS, and bottom two are *Chandra* spectra). Model results shown here are from fits performed independently on each detector's set of observations and with linked T and varying $N_{\rm H}$ and $R_{\rm em}$ between observations (for *Chandra*) and with linked $N_{\rm H}$ and varying T and $R_{\rm em}$ between observations (for *XMM-Newton*). Lower panel shows fit residuals. For clarity, only residuals for the 2014 ACIS, 2014 MOS, and 2013 pn observations are shown; other residuals are similar.

4.2 1WGA J1713.4−3949

Figure 2 shows spectra of 1WGA J1713.4−3949 from *Chandra* in 2000 and 2014, EPIC-MOS in 2001, 2004, and 2014, and EPIC-pn in 2004, 2013, and 2014. As noted in Section 3, the 2000 *Chandra* observation of the field of 1WGA J1713.4−3949 has the CCO located far off-axis (CCO on S1 chip is 23′ from ACIS-I aimpoint; see also Lazendic et al. 2003) and, as a result, the source's point-spread-function is significantly extended and distorted (hence the $1'\times2'$ diameter source extraction region; see Section 3). The CCO in the 2014 *Chandra* observation is also off-axis and distorted. These off-axis data are also not as well-calibrated. Therefore to minimize introducing additional systematic effects, we base our discussions and conclusions on results of fits to the *XMM-Newton* spectra of 1WGA J1713.4−3949. Nevertheless we present fits of the *Chandra* spectra in Appendix A for the sake of completeness and to compare with results from previous works. Furthermore, here we consider *XMM-Newton* MOS and pn data separately; a joint analysis is presented in Appendix A.

Tables 5 and 6 show results of model fits of *XMM-Newton* MOS spectra at 0.2–7 keV and pn spectra at 0.3–10 keV, respectively. Fitting spectra with a single absorbed blackbody yields poor results. When all absorbed thermal model parameters ($N_{\rm H}$, T, and $R_{\rm em}$) are allowed to vary between all observations, the fit is still not good. Note that the blackbody fit parameters, e.g., $R_{\rm em} \sim 0.5$ km, are comparable to those obtained in a fit of only the 2001 *XMM-Newton* spectra (Cassam-Chenaï et al. 2004). On the other hand, good fits

Table 5. Results of fits to the 2001, 2004, and 2014 *XMM-Newton* EPIC-MOS spectra of 1WGA J1713.4−3949 at 0.2–7 keV. Along with `tbabs`, fits are performed using model `bbodyrad`, `nsatmos`, `nsx`, or `nsmaxg` with model parameters free to vary between fits, unless given otherwise. Other model parameters are fixed at $M = 1.4\,M_\odot$, $R = 12$ km, and $d = 1.3$ kpc, unless otherwise noted. Absorbed 0.5–10 keV flux $f^{\rm abs}_{0.5-10}$ is in 10^{-13} erg cm^{-2} s^{-1}. Errors are 1σ.

Year	$N_{\rm H}$ (10^{21} cm^{-2})	T (10^6 K)	$R_{\rm em}/R$ or 1.3 kpc/d	$f^{\rm abs}_{0.5-10}$	χ^2/dof
		blackbody			
2001	$4.5^{+0.2}_{-0.2}$	$4.75^{+0.05}_{-0.05}$	$0.044^{+0.001}_{-0.001}$	$32.0^{+0.3}_{-0.4}$	1539/976
2004	$4.4^{+0.2}_{-0.2}$	$4.78^{+0.05}_{-0.05}$	$0.043^{+0.001}_{-0.001}$	$30.6^{+0.2}_{-0.4}$	
2014	$4.5^{+0.1}_{-0.1}$	$4.94^{+0.02}_{-0.02}$	$0.039^{+0.001}_{-0.001}$	$30.6^{+0.1}_{-0.2}$	
		`nsatmos` - non-magnetic hydrogen			
2001	$6.02^{+0.09}_{-0.06}$	$2.93^{+0.03}_{-0.04}$	$0.161^{+0.005}_{-0.003}$	$32.6^{+0.3}_{-0.4}$	1086/978
2004	—	$2.92^{+0.03}_{-0.04}$	$0.159^{+0.005}_{-0.003}$	$30.9^{+0.2}_{-0.3}$	
2014	—	$3.08^{+0.02}_{-0.02}$	$0.139^{+0.003}_{-0.002}$	$31.0^{+0.1}_{-0.1}$	
		`nsx` - non-magnetic carbon			
2001	$7.05^{+0.08}_{-0.06}$	$1.90^{+0.03}_{-0.04}$	$0.497^{+0.031}_{-0.021}$	$32.5^{+0.3}_{-0.4}$	1062/978
2004	—	$1.88^{+0.03}_{-0.04}$	$0.492^{+0.028}_{-0.020}$	$30.9^{+0.2}_{-0.4}$	
2014	—	$2.05^{+0.02}_{-0.02}$	$0.389^{+0.011}_{-0.008}$	$31.0^{+0.1}_{-0.1}$	
		`nsmaxg` - hydrogen at 10^{10} G ($R = 10$ km)			
2001	$6.28^{+0.07}_{-0.08}$	$3.20^{+0.03}_{-0.03}$	$0.174^{+0.004}_{-0.004}$	$32.6^{+0.3}_{-0.5}$	1089/978
2004	—	$3.17^{+0.03}_{-0.03}$	$0.172^{+0.004}_{-0.004}$	$30.9^{+0.2}_{-0.3}$	
2014	—	$3.34^{+0.02}_{-0.02}$	$0.154^{+0.002}_{-0.002}$	$30.9^{+0.1}_{-0.1}$	
		`nsmaxg` - hydrogen at 3×10^{13} G ($R = 10$ km)			
2001	$6.82^{+0.09}_{-0.08}$	$3.07^{+0.03}_{-0.04}$	$0.200^{+0.006}_{-0.005}$	$32.6^{+0.2}_{-0.4}$	1082/978
2004	—	$3.06^{+0.03}_{-0.03}$	$0.197^{+0.006}_{-0.005}$	$30.9^{+0.3}_{-0.4}$	
2014	—	$3.22^{+0.02}_{-0.02}$	$0.172^{+0.003}_{-0.003}$	$31.0^{+0.1}_{-0.2}$	

Table 6. Results of fits to the 2004, 2013, and 2014 *XMM-Newton* EPIC-pn spectra of 1WGA J1713.4−3949 at 0.3–10 keV. Along with `tbabs`, fits are performed using model `bbodyrad`, `nsatmos`, `nsx`, or `nsmaxg` with model parameters free to vary between fits, unless given otherwise. Other model parameters are fixed at $M = 1.4\,M_\odot$, $R = 12$ km, and $d = 1.3$ kpc, unless otherwise noted. Absorbed 0.5–10 keV flux $f^{\rm abs}_{0.5-10}$ is in 10^{-13} erg cm^{-2} s^{-1}. Errors are 1σ.

Year	$N_{\rm H}$ (10^{21} cm^{-2})	T (10^6 K)	$R_{\rm em}/R$ or 1.3 kpc/d	$f^{\rm abs}_{0.5-10}$	χ^2/dof
		blackbody			
2004	$4.72^{+0.15}_{-0.15}$	$4.70^{+0.05}_{-0.05}$	$0.045^{+0.001}_{-0.001}$	$30.4^{+0.2}_{-0.3}$	1873/1208
2013	$4.69^{+0.05}_{-0.05}$	$4.82^{+0.02}_{-0.02}$	$0.041^{+0.001}_{-0.001}$	$29.7^{+0.1}_{-0.1}$	
2014	$4.65^{+0.06}_{-0.06}$	$4.86^{+0.02}_{-0.02}$	$0.041^{+0.001}_{-0.001}$	$30.3^{+0.1}_{-0.1}$	
		`nsatmos` - non-magnetic hydrogen			
2004	$6.02^{+0.04}_{-0.05}$	$2.93^{+0.03}_{-0.03}$	$0.157^{+0.004}_{-0.003}$	$31.1^{+0.2}_{-0.3}$	1303/1210
2013	—	$3.01^{+0.01}_{-0.01}$	$0.146^{+0.002}_{-0.002}$	$30.2^{+0.1}_{-0.1}$	
2014	—	$3.03^{+0.02}_{-0.01}$	$0.144^{+0.002}_{-0.002}$	$30.7^{+0.1}_{-0.1}$	
		`nsx` - non-magnetic carbon			
2004	$7.06^{+0.04}_{-0.04}$	$1.90^{+0.03}_{-0.03}$	$0.485^{+0.025}_{-0.020}$	$31.1^{+0.1}_{-0.4}$	1285/1210
2013	—	$1.98^{+0.01}_{-0.01}$	$0.425^{+0.009}_{-0.009}$	$30.2^{+0.1}_{-0.2}$	
2014	—	$2.00^{+0.02}_{-0.02}$	$0.413^{+0.010}_{-0.009}$	$30.7^{+0.2}_{-0.2}$	
		`nsmaxg` - hydrogen at 3×10^{13} G ($R = 10$ km)			
2004	$6.70^{+0.04}_{-0.07}$	$3.10^{+0.03}_{-0.03}$	$0.190^{+0.004}_{-0.005}$	$31.2^{+0.2}_{-0.4}$	1368/1210
2013	—	$3.17^{+0.02}_{-0.01}$	$0.176^{+0.001}_{-0.003}$	$30.2^{+0.2}_{-0.1}$	
2014	—	$3.20^{+0.02}_{-0.01}$	$0.174^{+0.001}_{-0.003}$	$30.8^{+0.1}_{-0.2}$	

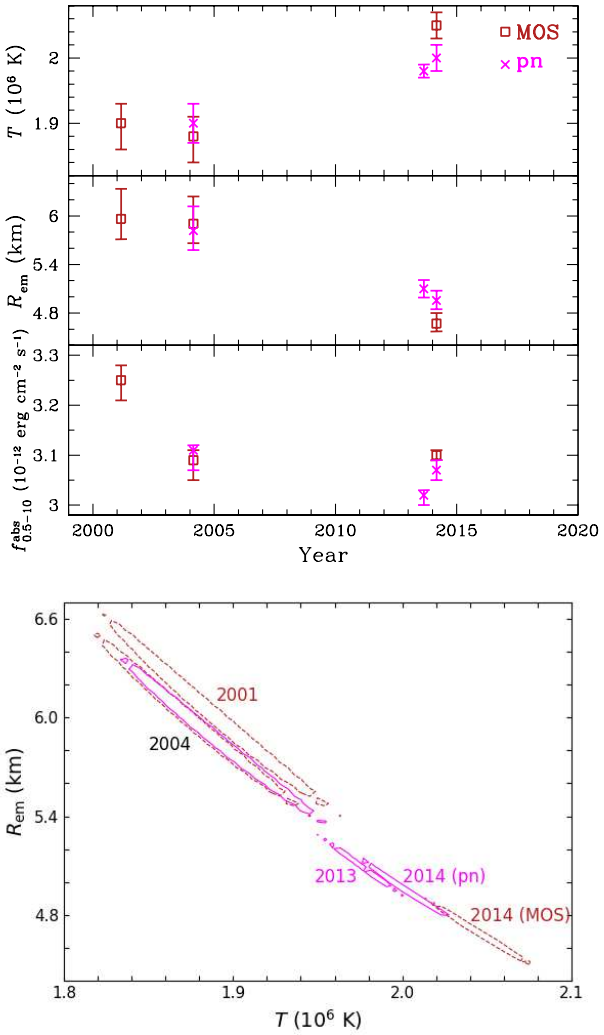

Figure 3. Top: Surface temperature T (upper), emission radius $R_{\rm em}$ (middle), and absorbed 0.5–10 keV flux $f^{\rm abs}_{0.5-10}$ (lower) of 1WGA J1713.4−3949 from non-magnetic carbon atmosphere model fits to *XMM-Newton* MOS (squares) and pn (crosses) spectra (see Tables 5 and 6). Errors are 1σ. Bottom: 90 percent confidence contours for T and $R_{\rm em}$ as measured using MOS (dashed) and pn (solid). Labels indicate observation year.

can be obtained with atmosphere model spectra such as those given in Table 3. Comparisons of fits where all parameters ($N_{\rm H}$, T, and $R_{\rm em}$) are linked or allowed to vary between observations indicate fits which allow for varying T and $R_{\rm em}$ are justified, e.g., for non-magnetic carbon model fits to pn spectra, we find F-test probabilities of 1×10^{-5} for linked parameters versus varying T and 4×10^{-3} for varying T versus varying T and $R_{\rm em}$, while for MOS spectra the F-test probabilities are 1×10^{-14} for linked parameters versus varying $N_{\rm H}$ and 4×10^{-4} for varying $N_{\rm H}$ versus varying T and $R_{\rm em}$. All atmosphere model fits give $N_{\rm H}\approx(6-7)\times10^{21}$ cm^{-2}, comparable to the SNR absorption. The best fit to both MOS and pn spectra are non-magnetic carbon atmospheres, but non-magnetic hydrogen are nearly as good ($\Delta\chi^2 = 24$ for 978 dof and $\Delta\chi^2 = 18$ for 1210 dof for MOS and pn, respectively). We note that Potekhin et al. (2020) use `nsx` to fit the 2014 pn spectrum and obtain similar results to our `nsx` fit results of the same spectrum (see Table 6). On the other hand, while low and high magnetic field hydrogen models yield similar quality MOS spectral fits to non-magnetic models (see examples in

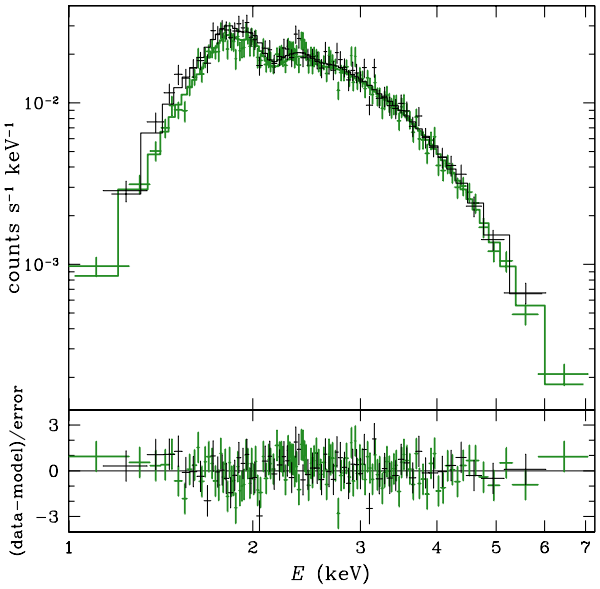

Figure 4. Upper panel shows *Chandra* spectra (black for 2009 and green for merged 2018 data) of XMMU J172054.5−372652 and absorbed non-magnetic carbon atmosphere model spectra. Model results shown here are from fits with all parameters linked between the two sets of observations. Lower panel shows fit residuals.

Table 5), these same magnetic models do not fit the pn spectra nearly as well. This can be attributed to the fact that magnetic models are softer than non-magnetic models for the same effective temperature (Shibanov et al. 1992) and the pn spectra here extends to 10 keV while MOS spectra only go up to 7 keV.

In Figure 3, we show the evolution of the MOS and pn inferred temperature T, emission radius $R_{\rm em}$, and absorbed flux $f^{\rm abs}_{0.5-10}$ for non-magnetic carbon atmosphere model fits (hydrogen atmosphere results show similar trends). Inferred values at the same or nearly the same epoch are consistent within $\sim 2\sigma$. A temperature increase of $\sim 4 \pm 2$ percent and emission radius decrease of $\sim 14 \pm 6$ percent are seen to occur between 2004 and 2013–14, while flux remains approximately constant. Also evident is an apparent flux drop, but without a significant change of temperature and emission radius, between 2001 and 2004.

4.3 XMMU J172054.5−372652

Figure 4 shows the 2009 and (merged) 2018 *Chandra* spectra of XMMU J172054.5−372652, and Table 7 shows results of model fits of these spectra at 0.9–7 keV. For the blackbody model, the fit yields a small hot spot ($R_{\rm em} \approx 0.8$ km for $d = 4.5$ kpc) that would suggest pulsations which are not detected despite searches (pulsed fraction limit of $\sim$ 30 percent for spin periods comparable to other CCOs; see Table 1). These blackbody results are in approximate agreement with those obtained in previous studies of the 2009 *Chandra* spectrum (Lovchinsky et al. 2011) and a 2007 *XMM-Newton* spectrum (Gaensler et al. 2008).

Comparable fits are achieved when an atmosphere model spectrum is used instead of a blackbody spectrum. The best-fit model is a magnetic ($B = 10^{13}$ G) partially ionized hydrogen atmosphere, with emission size $R_{\rm em} \approx 2.9$ km (for $R = 12$ km), although other magnetic hydrogen models at $B \geq 10^{12}$ G or a non-magnetic hydrogen model with $R_{\rm em} \approx 3.5$ km yield only slightly poorer fits ($\Delta\chi^2 \lesssim 4$) and are good fits to the observed spectra. A carbon atmosphere with $R_{\rm em} \approx 9.2$ km is a slightly worse fit compared to the best-fit model ($\Delta\chi^2 \approx 4$). We also note that the inferred absorption $N_{\rm H} \approx (5.3 - 5.6) \times 10^{22}$ cm^{-2} is somewhat greater than $N_{\rm H} \approx (3 - 4) \times 10^{22}$ cm^{-2} from spectral analysis of the SNR using *Chandra* (Gaensler et al. 2008), *Suzaku* (Yasumi et al. 2014), and *XMM-Newton* (Lovchinsky et al. 2011).

The spectral fit results shown in Table 7 assume the nominal distance to XMMU J172054.5−372652 of 4.5 kpc, which is determined from what appears to be interaction between a molecular cloud and SNR G350.1−0.3 (Gaensler et al. 2008). On the other hand, H I absorption towards the SNR gives a distance range of 4.5–10.7 kpc (Gaensler et al. 2008). Taking into account the considerations described in Section 4.1, we determine that the distance to XMMU J172054.5−372652 is 5.9 ± 0.7 kpc if the CCO has a carbon atmosphere with emission size $R_{\rm em} = R$, while a hydrogen atmosphere is possible if the hot region covers ~40 percent of the neutron star surface at a maximum distance to the CCO of 10.7 kpc. We note that Potekhin et al. (2020) fit the early epoch *Chandra* spectrum with a carbon atmosphere model via `nsx` and obtain a comparable distance of $6.1^{+2.6}_{-1.9}$ kpc.

Finally we examine whether there is evolution of model parameters from fits of the 2009 and 2018 spectra. We find there is very little change in the fit statistics (i.e., $\Delta\chi^2 < 2$; see, e.g., Section 5.1) when allowing $N_{\rm H}$, T, and/or $R_{\rm em}$ to vary between these data, and thus the spectral model parameters do not appear to vary significantly between observations.

4.4 Cassiopeia A

To account for a correlation between M, R, and `pileup` grade migration parameter α (see Shternin et al. 2021), we iterate initially between two model fits to the *Chandra* ACIS-S Graded spectra of the CCO in Cassiopeia A. The first fit allows for varying M and R (with the same values for all 14 observations) and fixed α_1 (for observations with frame time of 3.24 s; see Table 2) and α_2 (for observations with frame time of 3.04 s). The second fit allows for varying α_1 and α_2 and fixed M and R. Both fits allow for varying $N_{\rm H}$ (but tied across and hence the same value for all observations) and T (can be different for each observation). The best-fit converges to $M = 1.69\,M_{\rm Sun}$, $R = 13.0$ km, and $N_{\rm H} = 1.67^{+0.02}_{-0.06} \times 10^{22}$ cm^{-2}, which are nearly the same as values found in Wijngaarden et al. (2019), and $\alpha_1 = 0.33 \pm 0.03$ and $\alpha_2 = 0.24 \pm 0.02$, which are consistent with values found in Heinke & Ho (2010); Ho et al. (2015); Shternin et al. (2021). Figure 5 shows the M-R confidence contours.

Our final spectral fits allow for a varying surface temperature T between each observation and either assumes a constant absorption $N_{\rm H} = 1.67 \times 10^{22}$ cm^{-2} or allows $N_{\rm H}$ to vary between each observation, while holding M, R, α_1, and α_2 at the best-fit values from above. Results are given in Table 8 and Figures 6 and 7. A F-fest between the fits with a constant and varying $N_{\rm H}$ yields a probability of 0.02, so allowing $N_{\rm H}$ to vary is possibly preferred. The ten-year cooling rates of 2.2 ± 0.2 percent for constant $N_{\rm H}$ and 2.8 ± 0.3 percent for varying $N_{\rm H}$ are consistent with those from Wijngaarden et al. (2019) and cooling rate upper limits of 2.4 percent for constant $N_{\rm H}$ and 3.3 percent for varying $N_{\rm H}$ from Posselt & Pavlov (2018).

5 DISCUSSION

In this work, we analyze *Chandra* and *XMM-Newton* CCD spectra taken over one or two decades of four of the youngest CCOs known, CXOU J160103.1−513353 in G330.2+1.0 with an age of $<$ 1000 yr, 1WGA J1713.4−3949 in G347.3−0.5 with an age of

Table 7. Results of fits to the 2009 and (merged) 2018 *Chandra* spectra of XMMU J172054.5−372652 at 0.9–7 keV. Along with `pileup` and `tbabs`, fits are performed using model `bbodyrad`, `nsatmos`, `nsx`, or `nsmaxg` with model parameters linked between 2009 and 2018 fits, unless given otherwise. Other model parameters are fixed at $M = 1.4\,M_\odot$, $R = 12$ km, and $d = 4.5$ kpc. Errors are 1σ.

Year	α	$N_{\rm H}$ (10^{22} cm^{-2})	T (10^6 K)	$R_{\rm em}/R$ or 4.5 kpc$/d$	$f^{\rm abs}_{0.5-10}$ (10^{-13} erg cm^{-2} s^{-1})	χ^2/dof
			blackbody			
2009	$0.42^{+0.10}_{-0.09}$	$4.7^{+0.1}_{-0.1}$	$5.85^{+0.09}_{-0.09}$	$0.066^{+0.003}_{-0.001}$	$5.6^{+0.2}_{-0.2}$	150.4/178
2018	$0.34^{+0.06}_{-0.06}$	—	—	—	$5.4^{+0.1}_{-0.1}$	
			`nsatmos` - non-magnetic hydrogen			
2009	$0.19^{+0.10}_{-0.10}$	$5.4^{+0.1}_{-0.1}$	$3.45^{+0.09}_{-0.08}$	$0.29^{+0.02}_{-0.02}$	$5.4^{+0.2}_{-0.3}$	154.3/178
2018	$0.12^{+0.06}_{-0.06}$	—	—	—	$5.3^{+0.1}_{-0.2}$	
			`nsx` - non-magnetic carbon			
2009	$0.25^{+0.09}_{-0.10}$	$5.6^{+0.1}_{-0.1}$	$2.33^{+0.08}_{-0.08}$	$0.77^{+0.10}_{-0.08}$	$5.4^{+0.2}_{-0.3}$	154.2/178
2018	$0.18^{+0.06}_{-0.06}$	—	—	—	$5.3^{+0.1}_{-0.2}$	
			`nsmaxg` - hydrogen at 10^{13} G			
2009	$0.41^{+0.09}_{-0.09}$	$5.3^{+0.1}_{-0.1}$	$3.77^{+0.11}_{-0.10}$	$0.24^{+0.02}_{-0.02}$	$5.6^{+0.1}_{-0.3}$	150.4/178
2018	$0.33^{+0.05}_{-0.06}$	—	—	—	$5.4^{+0.1}_{-0.2}$	

Table 8. Results of fits to *Chandra* ACIS-S Graded spectra of the CCO in Cassiopeia A. Two spectral fit results using `nsx` are shown, one with constant $N_{\rm H}$ and one with varying $N_{\rm H}$. Other model parameters are fixed at $M = 1.69\,M_\odot$, $R = 13$ km, $d = 3.4$ kpc, and $\alpha = 0.33$ or 0.24 for observations with a frame time of 3.24 s (i.e., ObsIDs 114, 1952, and 5196; see Table 2) or 3.04 s, respectively. Each set of 14 temperatures and absorbed 0.5-7 keV fluxes $f^{\rm abs}_{0.5-7}$ are fit to a linear decline, with decline rate and fit statistic as shown. For merged ObsIDs, the MJD listed is that of the first ObsID. Error bars are 1σ.

		$N_{\rm H}$	1.67×10^{22} cm^{-2}		see below		
		χ^2/dof	1654/1641		1627/1627		
ObsID	Date	MJD	T (10^6 K)	$f^{\rm abs}_{0.5-7}$ (10^{-13} erg cm^{-2} s^{-1})	T (10^6 K)	$f^{\rm abs}_{0.5-7}$ (10^{-13} erg cm^{-2} s^{-1})	$N_{\rm H}$ (10^{22} cm^{-2})
114	2000 Jan 30	51573.4	$1.866^{+0.007}_{-0.008}$	$7.5^{+0.2}_{-0.1}$	$1.873^{+0.009}_{-0.010}$	$7.5^{+0.2}_{-0.1}$	$1.71^{+0.03}_{-0.04}$
1952	2002 Feb 6	52311.3	$1.859^{+0.007}_{-0.008}$	$7.4^{+0.2}_{-0.2}$	$1.869^{+0.010}_{-0.009}$	$7.4^{+0.1}_{-0.1}$	$1.73^{+0.04}_{-0.03}$
5196	2004 Feb 8	53043.7	$1.850^{+0.008}_{-0.006}$	$7.2^{+0.1}_{-0.1}$	$1.845^{+0.011}_{-0.008}$	$7.2^{+0.2}_{-0.1}$	$1.64^{+0.04}_{-0.03}$
9117/9773	2007 Feb 5/8	54439.9	$1.834^{+0.006}_{-0.010}$	$6.7^{+0.1}_{-0.1}$	$1.847^{+0.007}_{-0.013}$	$6.8^{+0.2}_{-0.1}$	$1.75^{+0.03}_{-0.05}$
10935/12020	2009 Nov 2/3	55137.9	$1.827^{+0.007}_{-0.009}$	$6.6^{+0.1}_{-0.1}$	$1.835^{+0.009}_{-0.012}$	$6.7^{+0.1}_{-0.2}$	$1.72^{+0.04}_{-0.04}$
10936/13177	2010 Oct 31/Nov 2	55500.2	$1.815^{+0.006}_{-0.008}$	$6.4^{+0.1}_{-0.1}$	$1.813^{+0.009}_{-0.012}$	$6.4^{+0.2}_{-0.1}$	$1.66^{+0.04}_{-0.04}$
14229	2012 May 15	56062.4	$1.793^{+0.007}_{-0.007}$	$6.2^{+0.1}_{-0.1}$	$1.800^{+0.011}_{-0.010}$	$6.3^{+0.1}_{-0.1}$	$1.71^{+0.05}_{-0.04}$
14480	2013 May 20	56432.6	$1.818^{+0.007}_{-0.007}$	$6.5^{+0.1}_{-0.1}$	$1.822^{+0.011}_{-0.010}$	$6.6^{+0.2}_{-0.1}$	$1.69^{+0.04}_{-0.04}$
14481	2014 May 12	56789.1	$1.800^{+0.008}_{-0.007}$	$6.2^{+0.2}_{-0.1}$	$1.807^{+0.011}_{-0.009}$	$6.3^{+0.1}_{-0.1}$	$1.71^{+0.04}_{-0.04}$
14482	2015 Apr 30	57142.5	$1.796^{+0.007}_{-0.007}$	$6.2^{+0.1}_{-0.1}$	$1.785^{+0.010}_{-0.010}$	$6.2^{+0.1}_{-0.2}$	$1.59^{+0.04}_{-0.04}$
19903/18344	2016 Oct 20/21	57681.2	$1.795^{+0.008}_{-0.006}$	$6.2^{+0.1}_{-0.1}$	$1.780^{+0.010}_{-0.009}$	$6.1^{+0.1}_{-0.1}$	$1.57^{+0.04}_{-0.04}$
19604	2017 May 16	57889.7	$1.801^{+0.008}_{-0.006}$	$6.4^{+0.1}_{-0.1}$	$1.797^{+0.012}_{-0.009}$	$6.3^{+0.1}_{-0.1}$	$1.64^{+0.05}_{-0.04}$
19605	2018 May 15	58253.7	$1.798^{+0.008}_{-0.006}$	$6.3^{+0.1}_{-0.2}$	$1.780^{+0.011}_{-0.009}$	$6.3^{+0.1}_{-0.2}$	$1.54^{+0.05}_{-0.04}$
19606	2019 May 13	58616.5	$1.788^{+0.008}_{-0.006}$	$6.2^{+0.2}_{-0.1}$	$1.784^{+0.011}_{-0.010}$	$6.2^{+0.1}_{-0.1}$	$1.64^{+0.05}_{-0.05}$
	10-year decline rate		$2.2 \pm 0.2\%$	$10 \pm 1\%$	$2.8 \pm 0.3\%$	$11 \pm 1\%$	
	χ^2/dof		13.4/12	14.7/12	10.0/12	12.2/12	

1500–2300 yr, XMMU J172054.5−372652 in G350.1−0.3 with an age of < 600 yr, and Cassiopeia A with an age of 340 yr. Spectra of each CCO can be well-described by neutron star atmosphere models. For CXOU J160103.1−513353, the spectral fits do not allow us to distinguish between a non-magnetic carbon atmosphere or a hydrogen atmosphere at magnetic fields $B \leq 7 \times 10^{10}$ G or $B \geq 10^{12}$ G. For 1WGA J1713.4−3949, the best-fit spectral model is a non-magnetic atmosphere composed of carbon or possibly hydrogen. For XMMU J172054.5−372652, the best-fit model is a magnetic ($B \geq 10^{13}$ G) hydrogen atmosphere, although non-magnetic hydrogen or carbon atmosphere spectra yield nearly as good fits to observed spectra. For Cassiopeia A, a non-magnetic carbon atmosphere spectrum continues to be a good fit to the spectra of the CCO.

Based purely on quality of fits of atmosphere model spectra to observed spectra obtained here, one composition is not preferred over another for the three older CCOs. The primary differences in fit results when the atmosphere is composed of carbon instead of hydrogen are a ~ 40 percent lower temperature and ~ 3 times larger emission radius (to maintain nearly constant $R^2_{\rm em}T^4$). The larger $R_{\rm em}$ could be an argument in favor of carbon because it is closer to the neutron star radius R, which would imply that the entire surface is essentially at a single temperature and would explain non-detection thus far of pulsations from each of these three CCOs. However, a hot region with radius 3–4 times smaller than R can still produce a pulsed fraction below current limits of 20–40 percent in the spin period range $0.1 - 0.4$ s of known CCOs (see Section 1; for pulsed fraction dependence on spot

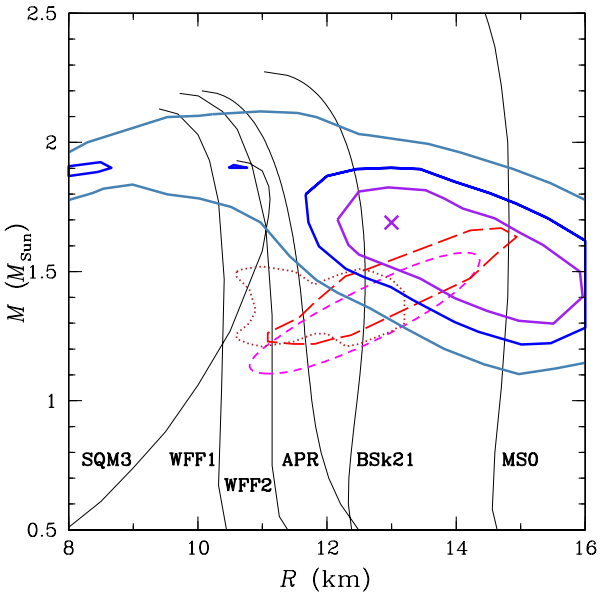

Figure 5. Neutron star mass M and radius R. Solid lines are 1σ, 90 percent, and 99 percent confidence contours obtained from fitting *Chandra* ACIS-S Graded spectra of the neutron star in the Cassiopeia A supernova remnant, assuming $N_{\rm H}$ does not vary between observations. Cross marks the best-fitting $M = 1.69\,M_{\rm Sun}$ and $R = 13.0$ km. Long-dashed, short-dashed, and dotted lines indicate M–R constraints at 1σ of millisecond pulsar PSR J0030+0451 from Miller et al. (2019) and Riley et al. (2019) and of GW170817 from Abbott et al. (2018), respectively. The light solid lines indicate the M–R relation obtained from a sample of theoretical nuclear equations of state, in particular, APR (Akmal et al. 1998), BSk21 (Potekhin et al. 2013), and MS0, SQM3, WFF1, and WFF2 (see Lattimer & Prakash 2001, and references therein).

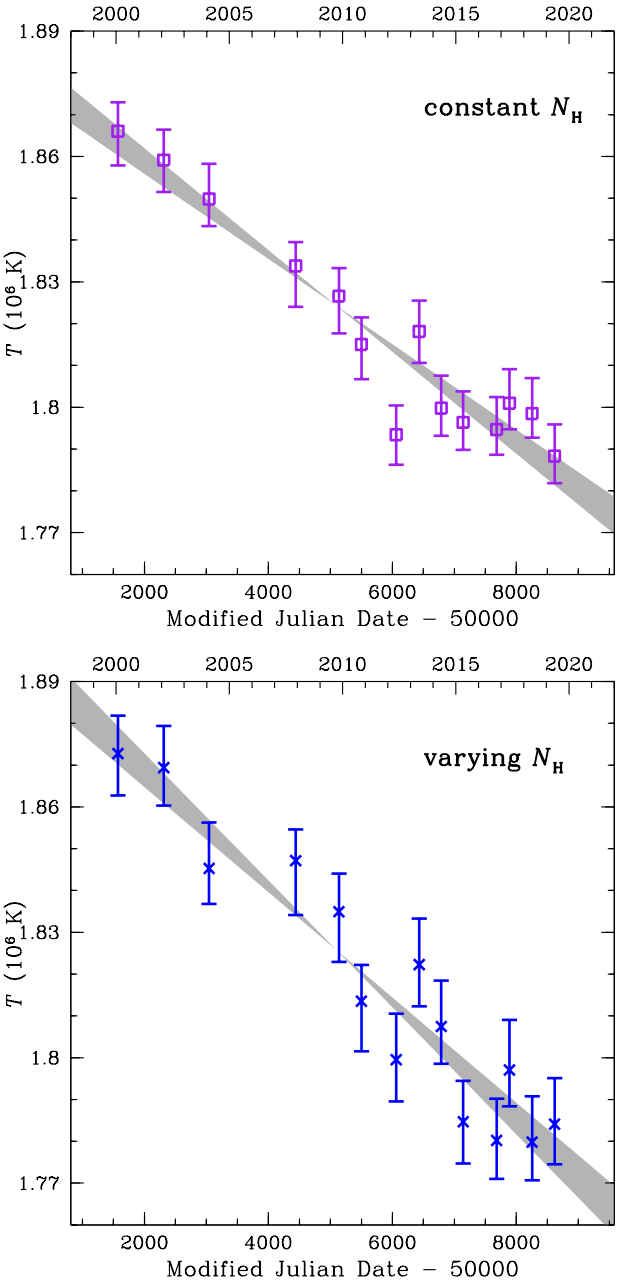

Figure 6. Surface temperature T of the neutron star in the Cassiopeia A supernova remnant as measured from *Chandra* ACIS-S Graded spectra over the past two decades. Data points indicate T obtained using the best-fitting neutron star mass $M = 1.69\,M_{\rm Sun}$ and radius $R = 13$ km and a constant absorption column $N_{\rm H} = 1.67 \times 10^{22}$ cm^{-2} (top panel) and varying $N_{\rm H}$ (bottom panel). Error bars are 1σ. Shaded regions show the uncertainty range for a linear fit to each set of T, i.e, a ten-year decline rate of 2.2 ± 0.2 percent for constant $N_{\rm H}$ and 2.8 ± 0.3 percent for varying $N_{\rm H}$, with the fit centered at the mid-point of all observations (MJD 55095).

size, see, e.g., Psaltis et al. 2000; DeDeo et al. 2001; Weinberg et al. 2001; Bogdanov et al. 2008; Lamb et al. 2009; Bauböck et al. 2015; Elshamouty et al. 2016). For example, Gotthelf et al. (2010) find that a model which includes a hot spot with $R_{\rm em}/R \sim 0.4$ (and a second smaller spot) is able to produce a pulsed fraction that matches the 11 percent measured for the CCO in Puppis A. Also of note is the stronger limit on the Cassiopeia A CCO pulsed fraction of 12 percent for $P > 0.01$ s compared to the other CCOs (see Table 1). Meanwhile, a hydrogen atmosphere is a natural consequence of even a very low-level of accretion from the interstellar medium on to a relatively cool neutron star surface several hundred years after neutron star formation (see Section 5.1 for further discussion). Thus from an evolution standpoint, a hydrogen atmosphere for the older CCOs studied here might be preferred. Future measurements of pulsations or improvements to pulsation constraints could provide stronger indications of their atmosphere composition.

5.1 Early evolution of CCOs

Hereafter we assume the four CCOs studied here are born similar to one another, even though their intrinsic properties and evolution must vary somewhat. This assumption enables us to use each as a snapshot of what a prototypical CCO might look like at different stages in its evolution. The ages derived for SNRs G330.2+1.0 and G350.1−0.3 are based on expansion of ejecta/shell material at constant velocity, and since deceleration is likely to occur, their ages are upper limits (Borkowski et al. 2018, 2020). Nevertheless for simplicity, we will consider these ages to be accurate, such that Cassiopeia A is the youngest CCO of the four at 340 yr old, XMMU J172054.5−372652 is the next youngest at 600 yr old, and CXOU J160103.1−513353 is 1000 yr old. 1WGA J1713.4−3949 is the oldest of the four, with an age of 1500–2300 yr. Note that the other three CCOs highlighted in Section 1 are much older, with ages > 4000 yr (Roger et al. 1988; Sun et al. 2004; Mayer et al. 2020).

While the youngest CCO, Cassiopeia A, likely has a carbon atmosphere, the three older CCOs studied in the present work might

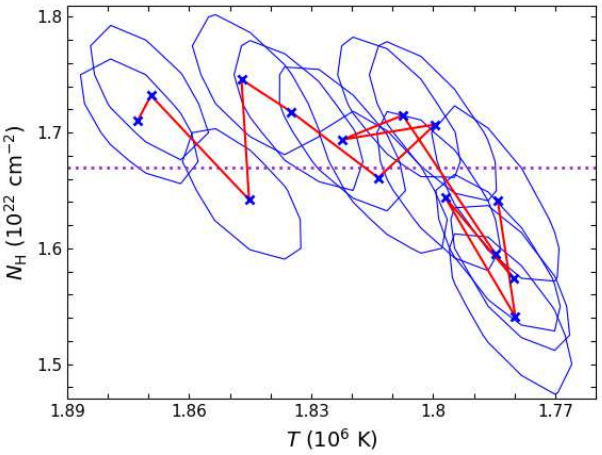

Figure 7. Absorption column N_H and surface temperature T as measured from a fit to *Chandra* ACIS-S Graded spectra of the Cassiopeia A neutron star. Crosses and 1σ confidence contours indicate N_H–T fit values using the best-fitting neutron star mass $M = 1.69\,M_{Sun}$ and radius $R = 13$ km, with lines connecting consecutive observations, while the horizontal dotted line indicates constant $N_H = 1.67 \times 10^{22}$ cm^{-2} used in the other spectral fit (see Figure 6).

have a hydrogen atmosphere, especially given the relatively weak pulsation constraint for each of these three. This evolution in atmosphere composition is due initially to the hot neutron star at birth. The high temperatures prompt formation of carbon and other heavy elements from nuclear fusion of any residual surface hydrogen and helium (Chang & Bildsten 2003, 2004; Chang et al. 2010; Wijngaarden et al. 2019, 2020). These nuclear reactions cease to be effective after several hundred years as the neutron star surface cools. Then even a small amount of accretion from the interstellar medium leads to sufficient hydrogen to form an optically thick atmosphere (Blaes et al. 1992; Wijngaarden et al. 2019).

Due to their high core temperatures at birth, neutron stars cool predominantly by neutrino emission at ages $\lesssim 10^6$ yr (Potekhin et al. 2015). The most rapid changes of surface temperature occur early, first when the temperature of the outer layers achieves equilibrium with the rapidly cooling core at an age of $\lesssim 100$ yr (Lattimer et al. 1994; Gnedin et al. 2001; see also Nomoto & Tsuruta 1987) and then when the temperature drops below the critical temperature for core neutrons to become superfluid, which activates the efficient neutrino emission process of Cooper pair formation and breaking (Gusakov et al. 2004; Page et al. 2004). The rapid cooling of the CCO in Cassiopeia A (at a ten-year rate of $\approx 2.2 \pm 0.2$ or 2.8 ± 0.3 percent, depending on whether N_H varies between observations) indicates the latter starts to take place at an age of ~ 200 yr (Page et al. 2011; Shternin et al. 2011). Neutron star cooling models predict that by an age of several hundred years, the cooling rate will be < 1 percent per decade. From the 1σ temperature uncertainties of our fit results with model parameters linked between observations (see Tables 4 and 7), we estimate upper limits on the ten-year cooling rates of 6 percent for XMMU J172054.5−372652 and 17 percent for CXOU J160103.1−513353. We measure a possible increase in temperature of $\sim 4 \pm 2$ percent (accompanied by a decrease in emission area; see Table 5 and 6) for 1WGA J1713.4−3949. We also perform fits of the spectra of XMMU J172054.5−372652 and CXOU J160103.1−513353 which allow the temperature to be different between each observation, and the results are shown in Table 9 and Figure 8 (analogous results for 1WGA J1713.4−3949 are shown in Figure 3). We point out that we are concerned in Figure 8 with relative changes in temperature and not in absolute temperature differences between CCOs since absolute temperatures depend on a variety of factors that are intrinsic to each CCO and may be different among CCOs in our sample, e.g., mass (and hence neutrino cooling rate) and radius (and hence gravitational redshift) and envelope composition and thickness. Nevertheless it is noteworthy that the temperatures of all three older CCOs appear to be higher than those of Cassiopeia A. Unlike for the 340 yr old CCO in Cassiopeia A, we do not see that temperatures of the 600 yr old XMMU J172054.5−372652 and 1000 yr old CXOU J160103.1−513353 are changing, at least within measurement uncertainties.

Table 9. Results of fits to *Chandra* spectra of CXOU J160103.1−513353 and XMMU J172054.5−372652 using a non-magnetic carbon atmosphere model (`nsx`) and allowing T to vary between the two epochs of observation, while N_H and R_{em} are linked. For XMMU J172054.5−372652, pile-up parameter $\alpha = 0.24^{+0.10}_{-0.10}$ and $0.18^{+0.06}_{-0.06}$ for the 2009 and 2018 fits, respectively. Other model parameters are fixed at $M = 1.4\,M_\odot$, $R = 12$ km, and $d = 5$ kpc for CXOU J160103.1−513353 and $d = 4.5$ kpc for XMMU J172054.5−372652. Absorbed 0.5–10 keV flux $f^{abs}_{0.5-10}$ is in 10^{-13} erg cm^{-2} s^{-1}. Errors are 1σ.

Year	N_H (10^{22} cm^{-2})	T (10^6 K)	R_{em}/R	$f^{abs}_{0.5-10}$	χ^2/dof
		CXOU J160103.1−513353			
2006	$4.8^{+0.3}_{-0.3}$	$1.9^{+0.2}_{-0.1}$	$0.75^{+0.25}_{-0.17}$	$1.5^{+0.1}_{-0.4}$	83.5/66
2017	—	$1.9^{+0.2}_{-0.1}$	—	$1.4^{+0.1}_{-0.3}$	
		XMMU J172054.5−372652			
2009	$5.6^{+0.1}_{-0.1}$	$2.34^{+0.08}_{-0.08}$	$0.77^{+0.10}_{-0.08}$	$5.4^{+0.2}_{-0.4}$	154.1/177
2018	—	$2.33^{+0.08}_{-0.08}$	—	$5.3^{+0.1}_{-0.3}$	

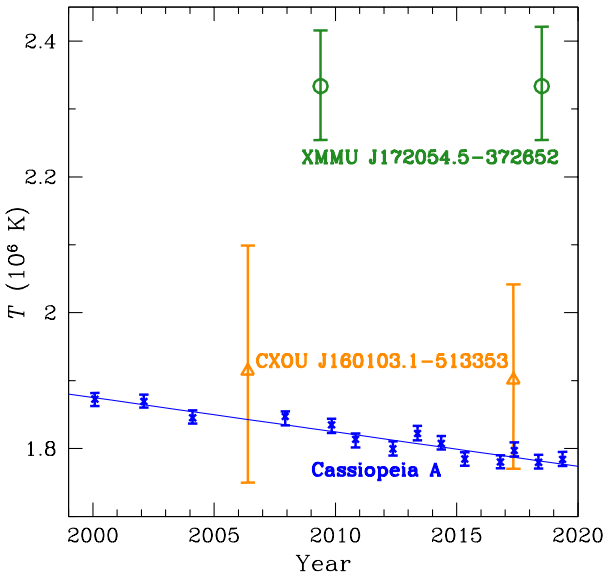

Figure 8. Surface temperature T of CXOU J160103.1−513353 (triangles) and XMMU J172054.5−372652 (circles) from non-magnetic carbon atmosphere model fits to *Chandra* spectra (see Table 9); see Figure 3 for 1WGA J1713.4−3949. Temperatures of the CCO in Cassiopeia A (crosses) are from the carbon atmosphere model fit with varying N_H (see Table 8); line shows the best-fit linear decline rate of 2.8 percent per decade. Errors are 1σ.

From our spectral fits, we find a non-magnetic carbon or hydrogen atmosphere provides a good model for the four youngest known CCOs: Cassiopeia A, XMMU J172054.5−372652, CXOU J160103.1−513353, and 1WGA J1713.4−3949. For the oldest of these four, 1WGA J1713.4−3949, a relatively low but slowly increasing magnetic field could explain its (possibly) increasing temperature, as its shrinking hot spot compresses the magnetic flux and heat from the interior is conducted along the growing magnetic field. It is also interesting to note that an outlier signal detected in gravitational wave searches of 1WGA J1713.4−3949 would imply a magnetic field $\sim 6 \times 10^{11}$ G, assuming that the frequency of the signal is the spin frequency of the CCO (Papa et al. 2020). One can also consider the three (older) CCOs with a measured spin period and spin period derivative that indicate a global dipolar magnetic field strength of $3 \times 10^{10} - 10^{11}$ G. Two of these three have hot spot emission that might indicate much stronger localized fields (Gotthelf et al. 2010; Shabaltas & Lai 2012; Bogdanov 2014), while the third undergoes spin frequency glitches, which are phenomena seen in many young pulsars with stronger fields (Gotthelf & Halpern 2020). Magnetic field evolution in the above CCOs can follow from a scenario where a strong global magnetic field at birth is submerged below the neutron star surface and gradually diffuses to the surface with an emergence timescale that depends on burial depth and can be $\sim$ 1000 yr (Ho 2011, 2015; Viganò & Pons 2012; Torres-Forné et al. 2016; Fraija et al. 2018; Gourgouliatos et al. 2020)

Previous and future searches for CCOs and their descendants (Gotthelf et al. 2013b; Bogdanov et al. 2014; Luo et al. 2015; Pires 2018) will be important for revealing where the CCO class sits within the general population of neutron stars. As we show here, studies of CCOs can potentially provide valuable insights into the surface composition, magnetic field, and evolution of neutron stars.

ACKNOWLEDGEMENTS

We thank J. Lazendic-Galloway, D. Patnaude, and P. Slane for support in obtaining *Chandra* data used here. WCGH appreciates use of computer facilities at the Kavli Institute for Particle Astrophysics and Cosmology. COH acknowledges support from the Natural Sciences and Engineering Research Council of Canada (NSERC) via Discovery Grant RGPIN-2016-04602. DLK is supported by the NANOGrav Physics Frontiers Center through NSF award number 1430284. This research has made use of data obtained from the Chandra Data Archive and the Chandra Source Catalog, and software provided by the Chandra X-ray Center (CXC) in the application packages CIAO, ChIPS, and Sherpa. This research has made use of data and/or software provided by the High Energy Astrophysics Science Archive Research Center (HEASARC), which is a service of the Astrophysics Science Division at NASA/GSFC and the High Energy Astrophysics Division of the Smithsonian Astrophysical Observatory. The authors acknowledge use of the XMM-Newton Science Archive (XSA) for searching and downloading data.

DATA AVAILABILITY

The data underlying this article will be shared on reasonable request to the corresponding author.

REFERENCES

Abbott B. P., et al., 2018, Phys. Rev. Lett., 121, 161101
Acero F., Ballet J., Decourchelle A., Lemoine-Goumard M., Ortega M., Giacani E., Dubner G., Cassam-Chenaï G., 2009, A&A, 505, 157
Acero F., Katsuda S., Ballet J., Petre R., 2017, A&A, 597, A106
Akmal A., Pandharipande V. R., Ravenhall D. G., 1998, Phys. Rev. C, 58, 1804
Alcock C., Illarionov A., 1980, ApJ, 235, 534
Arnaud K. A., 1996, in Jacoby G. H., Barnes J., eds, Astronomical Society of the Pacific Conference Series Vol. 101, Astronomical Data Analysis Software and Systems V. p. 17
Bauböck M., Psaltis D., Özel F., 2015, ApJ, 811, 144
Bignami G. F., Caraveo P. A., De Luca A., Mereghetti S., 2003, Nature, 423, 725
Blaes O. M., Blandford R. D., Madau P., Yan L., 1992, ApJ, 399, 634
Blaschke D., Grigorian H., Voskresensky D. N., Weber F., 2012, Phys. Rev. C, 85, 022802
Bogdanov S., 2014, ApJ, 790, 94
Bogdanov S., Grindlay J. E., Rybicki G. B., 2008, ApJ, 689, 407
Bogdanov S., Ng C. Y., Kaspi V. M., 2014, ApJ, 792, L36
Bogdanov S., et al., 2019, ApJ, 887, L26
Bonanno A., Baldo M., Burgio G. F., Urpin V., 2014, A&A, 561, L5
Borkowski K. J., Reynolds S. P., Williams B. J., Petre R., 2018, ApJ, 868, L21
Borkowski K. J., Miltich W., Reynolds S. P., 2020, ApJ, 905, L19
Cassam-Chenaï G., Decourchelle A., Ballet J., Sauvageot J. L., Dubner G., Giacani E., 2004, A&A, 427, 199
Chang P., Bildsten L., 2003, ApJ, 585, 464
Chang P., Bildsten L., 2004, ApJ, 605, 830
Chang P., Bildsten L., Arras P., 2010, ApJ, 723, 719
Chevalier R. A., 1989, ApJ, 346, 847
Davis J. E., 2001, ApJ, 562, 575
De Luca A., 2008, in Bassa C., Wang Z., Cumming A., Kaspi V. M., eds, American Institute of Physics Conference Series Vol. 983, 40 Years of Pulsars: Millisecond Pulsars, Magnetars and More. pp 311–319, doi:10.1063/1.2900173
De Luca A., 2017, Journal of Physics Conference Series, 932, 012006
De Luca A., Mereghetti S., Caraveo P. A., Moroni M., Mignani R. P., Bignami G. F., 2004, A&A, 418, 625
DeDeo S., Psaltis D., Narayan R., 2001, ApJ, 559, 346
Doroshenko V., Suleimanov V., Santangelo A., 2018, A&A, 618, A76
Elshamouty K. G., Heinke C. O., Morsink S. M., Bogdanov S., Stevens A. L., 2016, ApJ, 826, 162
Fesen R. A., et al., 2006, ApJ, 645, 283
Fesen R. A., Kremer R., Patnaude D., Milisavljevic D., 2012, AJ, 143, 27
Fraija N., Bernal C. G., Morales G., Negreiros R., 2018, Phys. Rev. D, 98, 083012
Fruscione A., et al., 2006, Proceedings of SPIE, 6270, 62701V
Fukui Y., et al., 2003, PASJ, 55, L61
Gaensler B. M., et al., 2008, ApJ, 680, L37
Gnedin O. Y., Yakovlev D. G., Potekhin A. Y., 2001, MNRAS, 324, 725
Gotthelf E. V., Halpern J. P., 2020, ApJ, 900, 159
Gotthelf E. V., Perna R., Halpern J. P., 2010, ApJ, 724, 1316
Gotthelf E. V., Halpern J. P., Alford J., 2013a, ApJ, 765, 58
Gotthelf E. V., Halpern J. P., Allen B., Knispel B., 2013b, ApJ, 773, 141
Gourgouliatos K. N., Hollerbach R., Igoshev A. P., 2020, MNRAS, 495, 1692
Gusakov M. E., Kaminker A. D., Yakovlev D. G., Gnedin O. Y., 2004, A&A, 423, 1063
Halpern J. P., Gotthelf E. V., 2010, ApJ, 709, 436
Hamaguchi K., Nagata N., Yanagi K., Zheng J., 2018, Phys. Rev. D, 98, 103015
Hebbar P. R., Heinke C. O., Ho W. C. G., 2020, MNRAS, 491, 1585
Heinke C. O., Ho W. C. G., 2010, ApJ, 719, L167
Heinke C. O., Rybicki G. B., Narayan R., Grindlay J. E., 2006, ApJ, 644, 1090
Ho W. C. G., 2011, MNRAS, 414, 2567
Ho W. C. G., 2013, in van Leeuwen J., ed., International Astronomical Union Symposium Vol. 291, Neutron Stars and Pulsars: Challenges and Opportunities after 80 years. pp 101–106, doi:10.1017/S1743921312023289
Ho W. C. G., 2014, in Petit P., Jardine M., Spruit H. C., eds, International Astronomical Union Symposium Vol. 302, Magnetic Fields throughout Stellar Evolution. pp 435–438, doi:10.1017/S1743921314002683

Ho W. C. G., 2015, MNRAS, 452, 845
Ho W. C. G., Heinke C. O., 2009, Nature, 462, 71
Ho W. C. G., Potekhin A. Y., Chabrier G., 2008, ApJS, 178, 102
Ho W. C. G., Elshamouty K. G., Heinke C. O., Potekhin A. Y., 2015, Phys. Rev. C, 91, 015806
Katsuda S., et al., 2015, ApJ, 814, 29
Klochkov D., Pühlhofer G., Suleimanov V., Simon S., Werner K., Santangelo A., 2013, A&A, 556, A41
Klochkov D., Suleimanov V., Pühlhofer G., Yakovlev D. G., Santangelo A., Werner K., 2015, A&A, 573, A53
Klochkov D., Suleimanov V., Sasaki M., Santangelo A., 2016, A&A, 592, L12
Koo B. C., Kang J., McClure-Griffiths N., 2004, in Camilo F., Gaensler B. M., eds, International Astronomical Union Symposium Vol. 218, Young Neutron Stars and Their Environments. p. 85
Lamb F. K., Boutloukos S., Van Wassenhove S., Chamberlain R. T., Lo K. H., Clare A., Yu W., Miller M. C., 2009, ApJ, 706, 417
Lattimer J. M., Prakash M., 2001, ApJ, 550, 426
Lattimer J. M., van Riper K. A., Prakash M., Prakash M., 1994, ApJ, 425, 802
Lazendic J. S., Slane P. O., Gaensler B. M., Plucinsky P. P., Hughes J. P., Galloway D. K., Crawford F., 2003, ApJ, 593, L27
Leahy D. A., Ranasinghe S., Gelowitz M., 2020, ApJS, 248, 16
Leinson L. B., 2014, J. Cosmology Astropart. Phys., 2014, 031
Lovchinsky I., Slane P., Gaensler B. M., Hughes J. P., Ng C. Y., Lazendic J. S., Gelfand J. D., Brogan C. L., 2011, ApJ, 731, 70
Luo J., Ng C. Y., Ho W. C. G., Bogdanov S., Kaspi V. M., He C., 2015, ApJ, 808, 130
Mayer M., Becker W., Patnaude D., Winkler P. F., Kraft R., 2020, ApJ, 899, 138
McClure-Griffiths N. M., Green A. J., Dickey J. M., Gaensler B. M., Haynes R. F., Wieringa M. H., 2001, ApJ, 551, 394
Mignani R. P., Zaggia S., de Luca A., Perna R., Bassan N., Caraveo P. A., 2008, A&A, 484, 457
Miller M. C., et al., 2019, ApJ, 887, L24
Mori K., Ho W. C. G., 2007, MNRAS, 377, 905
Moriguchi Y., Tamura K., Tawara Y., Sasago H., Yamaoka K., Onishi T., Fukui Y., 2005, ApJ, 631, 947
Murray S. S., Ransom S. M., Juda M., Hwang U., Holt S. S., 2002, ApJ, 566, 1039
Negreiros R., Schramm S., Weber F., 2013, Physics Letters B, 718, 1176
Noda T., Hashimoto M.-a., Yasutake N., Maruyama T., Tatsumi T., Fujimoto M., 2013, ApJ, 765, 1
Nomoto K., Tsuruta S., 1987, ApJ, 312, 711
Page D., Lattimer J. M., Prakash M., Steiner A. W., 2004, ApJS, 155, 623
Page D., Prakash M., Lattimer J. M., Steiner A. W., 2011, Phys. Rev. Lett., 106, 081101
Papa M. A., et al., 2020, ApJ, 897, 22
Park S., Mori K., Kargaltsev O., Slane P. O., Hughes J. P., Burrows D. N., Garmire G. P., Pavlov G. G., 2006, ApJ, 653, L37
Park S., Kargaltsev O., Pavlov G. G., Mori K., Slane P. O., Hughes J. P., Burrows D. N., Garmire G. P., 2009, ApJ, 695, 431
Pavlov G. G., Luna G. J. M., 2009, ApJ, 703, 910
Pires A. M., 2018, in Weltevrede P., Perera B. B. P., Preston L. L., Sanidas S., eds, International Astronomical Union Symposium Vol. 337, Pulsar Astrophysics the Next Fifty Years. pp 112–115, doi:10.1017/S1743921317009590
Posselt B., Pavlov G. G., 2018, ApJ, 864, 135
Posselt B., Pavlov G. G., Suleimanov V., Kargaltsev O., 2013, ApJ, 779, 186
Potekhin A. Y., 2014, Physics Uspekhi, 57, 735
Potekhin A. Y., Fantina A. F., Chamel N., Pearson J. M., Goriely S., 2013, A&A, 560, A48
Potekhin A. Y., Chabrier G., Ho W. C. G., 2014, A&A, 572, A69
Potekhin A. Y., Pons J. A., Page D., 2015, Space Sci. Rev., 191, 239
Potekhin A. Y., Zyuzin D. A., Yakovlev D. G., Beznogov M. V., Shibanov Y. A., 2020, MNRAS, 496, 5052
Predehl P., Costantini E., Hasinger G., Tanaka Y., 2003, Astronomische Nachrichten, 324, 73
Psaltis D., Özel F., DeDeo S., 2000, ApJ, 544, 390
Ransom S. M., 2002, in Slane P. O., Gaensler B. M., eds, Astronomical Society of the Pacific Conference Series Vol. 271, Neutron Stars in Supernova Remnants. p. 361
Reed J. E., Hester J. J., Fabian A. C., Winkler P. F., 1995, ApJ, 440, 706
Riley T. E., et al., 2019, ApJ, 887, L21
Roger R. S., Milne D. K., Kesteven M. J., Wellington K. J., Haynes R. F., 1988, ApJ, 332, 940
Sanwal D., Pavlov G. G., Zavlin V. E., Teter M. A., 2002, ApJ, 574, L61
Sedrakian A., 2013, A&A, 555, L10
Shabaltas N., Lai D., 2012, ApJ, 748, 148
Shibanov I. A., Zavlin V. E., Pavlov G. G., Ventura J., 1992, A&A, 266, 313
Shternin P. S., Yakovlev D. G., Heinke C. O., Ho W. C. G., Patnaude D. J., 2011, MNRAS, 412, L108
Shternin P. S., Ofengeim D. D., Ho W. C. G., Heinke C. O., Wijngaarden M. J. P., Patnaude D. J., 2021, MNRAS, 506, 709
Slane P., Gaensler B. M., Dame T. M., Hughes J. P., Plucinsky P. P., Green A., 1999, ApJ, 525, 357
Suleimanov V. F., Klochkov D., Poutanen J., Werner K., 2017, A&A, 600, A43
Sun M., Seward F. D., Smith R. K., Slane P. O., 2004, ApJ, 605, 742
Tananbaum H., 1999, IAU Circ., 7246, 1
Taranto G., Burgio G. F., Schulze H. J., 2016, MNRAS, 456, 1451
Torii K., Uchida H., Hasuike K., Tsunemi H., Yamaguchi Y., Shibata S., 2006, PASJ, 58, L11
Torres-Forné A., Cerdá-Durán P., Pons J. A., Font J. A., 2016, MNRAS, 456, 3813
Tsuji N., Uchiyama Y., 2016, PASJ, 68, 108
Verner D. A., Ferland G. J., Korista K. T., Yakovlev D. G., 1996, ApJ, 465, 487
Viganò D., Pons J. A., 2012, MNRAS, 425, 2487
Wang Z. R., Qu Q. Y., Chen Y., 1997, A&A, 318, L59
Weinberg N., Miller M. C., Lamb D. Q., 2001, ApJ, 546, 1098
Wijngaarden M. J. P., Ho W. C. G., Chang P., Heinke C. O., Page D., Beznogov M., Patnaude D. J., 2019, MNRAS, 484, 974
Wijngaarden M. J. P., et al., 2020, MNRAS, 493, 4936
Williams B. J., Hewitt J. W., Petre R., Temim T., 2018, ApJ, 855, 118
Wilms J., Allen A., McCray R., 2000, ApJ, 542, 914
Yang S.-H., Pi C.-M., Zheng X.-P., 2011, ApJ, 735, L29
Yasumi M., Nobukawa M., Nakashima S., Uchida H., Sugawara R., Tsuru T. G., Tanaka T., Koyama K., 2014, PASJ, 66, 68

APPENDIX A: ADDITIONAL ANALYSES OF *Chandra* AND *XMM-Newton* DATA OF 1WGA J1713.4−3949

Here we present analyses of additional spectral data on 1WGA J1713.4−3949. These include *Chandra* observations that are significantly off-axis and distorted on the ACIS detectors, as discussed in Sections 3 and 4.2. Also presented is an analysis where we jointly fit *XMM-Newton* MOS and pn data, rather than treat each detector separately as done in Section 4.2.

Table A1 shows results of model fits of *Chandra* spectra at 0.3–7 keV. We find the pile-up grade migration parameter α to be unconstrained in fits of the spectra from 2000, and we leave it free to vary since it has an (small) effect on the uncertainties of other fit parameters. Note that the blackbody fit parameters, e.g., $R_{\rm em} \sim 1-3$ km, are comparable to those obtained in a joint fit of the 2000 *Chandra* spectrum and 2001 *XMM-Newton* spectra (Lazendic et al. 2003). Lazendic et al. (2003) obtain good fits with multi-component models that include a power law and either a non-magnetic hydrogen atmosphere (`nsspec`) or a magnetic ($B = 10^{12}$ G) fully ionized hydrogen atmosphere (`nsa`). Significantly improved single-component model fits are obtained after considering a wider range of atmosphere model spectra. Best fits are those that use a partially ionized hydrogen atmosphere model with $B \geq 4 \times 10^{12}$ G (see examples in Table A1), which result in a $N_{\rm H} \approx (7-9) \times 10^{21}$ cm^{-2} that is somewhat higher

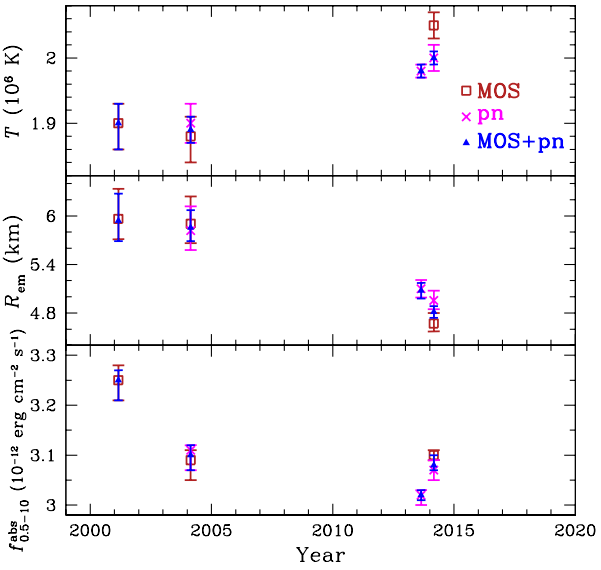

Figure A1. Surface temperature T (top), emission radius $R_{\rm em}$ (middle), and absorbed 0.5–10 keV flux $f^{\rm abs}_{0.5-10}$ (bottom) of 1WGA J1713.4−3949 from non-magnetic carbon atmosphere model fits to *XMM-Newton* MOS (squares) and pn (crosses) spectra independently (see Tables 5 and 6) and fits to MOS+pn (triangles) spectra jointly (see Table A2). Errors are 1σ.

than the SNR absorption $N_{\rm H} \approx 5 \times 10^{21}$ cm^{-2} near the CCO (see Section 1) and an emission region size $R_{\rm em} \geq 4$ km (for $R = 12$ km and $d = 1.3$ kpc). Atmosphere models with non-magnetic or low magnetic field ($B = 10^{10}$ G) hydrogen or non-magnetic carbon also provide good fits.

Table A2 shows results of joint model fits of *XMM-Newton* MOS spectra at 0.2–7 keV and pn spectra at 0.3–10 keV, respectively. Note that, in these joint fits, an extra fit parameter is introduced to account for a difference in relative normalization between MOS and pn spectra; this parameter is allowed to vary in fits of the 2004 and 2014 MOS and pn data, while it is fixed to 1 for the 2001 MOS and 2013 pn data. In Figure A1, we show the evolution of the MOS and pn inferred temperature T, emission radius $R_{\rm em}$, and absorbed flux $f^{\rm abs}_{0.5-10}$ for non-magnetic carbon atmosphere model fits. These results are very similar to those obtained in Section 4.2 where MOS and pn data are fit independently.

This paper has been typeset from a TEX/LATEX file prepared by the author.

Table A1. Results of fits to the 2000 and 2014 *Chandra* spectra of 1WGA J1713.4−3949 at 0.3–7 keV. Along with `pileup` and `tbabs`, fits are performed using model `bbodyrad`, `nsatmos`, `nsx`, or `nsmaxg` with model parameters free to vary between 2000 and 2014 fits, unless given otherwise. Other model parameters are fixed at $M = 1.4\,M_\odot$, $R = 12$ km, and $d = 1.3$ kpc, unless otherwise noted. Errors are 1σ.

Year	α	$N_{\rm H}$ (10^{21} cm^{-2})	T (10^6 K)	$R_{\rm em}/R$ or 1.3 kpc/d	$f^{\rm abs}_{0.5-10}$ (10^{-13} erg cm^{-2} s^{-1})	χ^2/dof
			blackbody			
2000	unconstrained	$6.0^{+0.2}_{-0.2}$	$4.37^{+0.06}_{-0.06}$	$0.25^{+0.01}_{-0.01}$	$31.2^{+0.6}_{-0.3}$	280.7/230
2014	$0.24^{+0.03}_{-0.03}$	$7.4^{+0.5}_{-0.5}$	$4.13^{+0.10}_{-0.10}$	$0.088^{+0.006}_{-0.006}$	$37.1^{+0.2}_{-1.0}$	
			`nsatmos` - non-magnetic hydrogen			
2000	unconstrained	$7.4^{+0.2}_{-0.2}$	$2.63^{+0.05}_{-0.05}$	$0.97^{+0.05}_{-0.04}$	$31.7^{+0.3}_{-0.7}$	248.5/231
2014	$0.09^{+0.02}_{-0.02}$	$9.1^{+0.2}_{-0.2}$	—	$0.30^{+0.01}_{-0.01}$	$37.1^{+0.3}_{-0.7}$	
			`nsx` - non-magnetic carbon			
2000	unconstrained	$8.1^{+0.1}_{-0.1}$	$1.62^{+0.06}_{-0.03}$	$3.7^{+0.3}_{-0.3}$	$31.9^{+0.1}_{-5.0}$	254.4/231
2014	$0.028^{+0.005}_{-0.006}$	$8.9^{+0.2}_{-0.2}$	—	$2.4^{+0.2}_{-0.2}$	$37.1^{+5.3}_{-2.9}$	
			`nsmaxg` - hydrogen at 10^{10} G ($R = 10$ km)			
2000	unconstrained	$7.6^{+0.2}_{-0.2}$	$2.90^{+0.05}_{-0.05}$	$1.03^{+0.05}_{-0.05}$	$31.7^{+0.3}_{-0.8}$	250.0/231
2014	$0.08^{+0.02}_{-0.02}$	$8.7^{+0.3}_{-0.2}$	—	$0.32^{+0.01}_{-0.01}$	$36.9^{+0.5}_{-0.7}$	
			`nsmaxg` - hydrogen at 10^{13} G			
2000	unconstrained	$8.2^{+0.2}_{-0.1}$	$2.67^{+0.05}_{-0.06}$	$1.03^{+0.07}_{-0.05}$	$31.7^{+0.2}_{-0.6}$	241.7/231
2014	$0.09^{+0.02}_{-0.01}$	$9.3^{+0.3}_{-0.3}$	—	$0.32^{+0.02}_{-0.01}$	$37.0^{+0.3}_{-0.5}$	

Table A2. Results of joint fits to the 2001, 2004, and 2014 *XMM-Newton* EPIC-MOS spectra at 0.2–7 keV and 2004, 2013, and 2014 *XMM-Newton* EPIC-pn spectra at 0.3–10 keV of 1WGA J1713.4−3949. Along with `tbabs` and a parameter to account for MOS and pn differences, fits are performed using model `bbodyrad`, `nsatmos`, `nsx`, or `nsmaxg` with model parameters free to vary between fits, unless given otherwise. Other model parameters are fixed at $M = 1.4\,M_\odot$, $R = 12$ km, and $d = 1.3$ kpc, unless otherwise noted. Absorbed 0.5–10 keV flux $f^{\rm abs}_{0.5-10}$ is in 10^{-13} erg cm^{-2} s^{-1}. Errors are 1σ.

Year	$N_{\rm H}$ (10^{21} cm^{-2})	T (10^6 K)	$R_{\rm em}/R$ or 1.3 kpc/d	$f^{\rm abs}_{0.5-10}$	MOS/pn	χ^2/dof
			blackbody			
2001	$4.51^{+0.19}_{-0.18}$	$4.75^{+0.05}_{-0.05}$	$0.0442^{+0.0014}_{-0.0013}$	$32.0^{+0.4}_{-0.3}$	—	3421/2188
2004	$4.58^{+0.11}_{-0.11}$	$4.73^{+0.04}_{-0.04}$	$0.0437^{+0.0009}_{-0.0008}$	$30.5^{+0.2}_{-0.4}$	$1.00^{+0.01}_{-0.01}$	
2013	$4.68^{+0.05}_{-0.05}$	$4.82^{+0.02}_{-0.02}$	$0.0414^{+0.0004}_{-0.0004}$	$29.7^{+0.1}_{-0.1}$	—	
2014	$4.57^{+0.05}_{-0.05}$	$4.90^{+0.02}_{-0.01}$	$0.0402^{+0.0003}_{-0.0003}$	$30.4^{+0.2}_{-0.1}$	$1.000^{+0.005}_{-0.005}$	
			`nsatmos` - non-magnetic hydrogen			
2001	$6.01^{+0.04}_{-0.04}$	$2.93^{+0.03}_{-0.04}$	$0.161^{+0.005}_{-0.003}$	$32.6^{+0.2}_{-0.4}$	—	2396/2191
2004	—	$2.93^{+0.02}_{-0.02}$	$0.158^{+0.003}_{-0.002}$	$31.0^{+0.3}_{-0.3}$	$1.00^{+0.01}_{-0.01}$	
2013	—	$3.01^{+0.01}_{-0.01}$	$0.146^{+0.002}_{-0.001}$	$30.2^{+0.1}_{-0.1}$	—	
2014	—	$3.06^{+0.01}_{-0.01}$	$0.142^{+0.001}_{-0.001}$	$30.9^{+0.1}_{-0.2}$	$1.000^{+0.005}_{-0.005}$	
			`nsx` - non-magnetic carbon			
2001	$7.05^{+0.04}_{-0.04}$	$1.90^{+0.03}_{-0.04}$	$0.495^{+0.028}_{-0.021}$	$32.5^{+0.2}_{-0.4}$	—	2354/2191
2004	—	$1.89^{+0.02}_{-0.02}$	$0.488^{+0.018}_{-0.014}$	$31.0^{+0.2}_{-0.3}$	$1.00^{+0.01}_{-0.01}$	
2013	—	$1.98^{+0.01}_{-0.01}$	$0.423^{+0.008}_{-0.008}$	$30.2^{+0.1}_{-0.1}$	—	
2014	—	$2.00^{+0.01}_{-0.01}$	$0.401^{+0.006}_{-0.006}$	$30.8^{+0.2}_{-0.1}$	$0.999^{+0.005}_{-0.005}$	
			`nsmaxg` - hydrogen at 3×10^{13} G ($R = 10$ km)			
2001	$6.73^{+0.03}_{-0.05}$	$3.09^{+0.03}_{-0.03}$	$0.196^{+0.005}_{-0.005}$	$32.6^{+0.3}_{-0.3}$	—	2458/2191
2004	—	$3.08^{+0.02}_{-0.02}$	$0.193^{+0.003}_{-0.003}$	$31.1^{+0.3}_{-0.3}$	$1.00^{+0.01}_{-0.01}$	
2013	—	$3.17^{+0.02}_{-0.01}$	$0.177^{+0.001}_{-0.002}$	$30.2^{+0.2}_{-0.1}$	—	
2014	—	$3.21^{+0.02}_{-0.01}$	$0.173^{+0.001}_{-0.002}$	$30.9^{+0.1}_{-0.1}$	$0.998^{+0.005}_{-0.005}$	